



UNIVERSITY OF CRETE

DEPARTMENT OF PHYSICS

MSc THESIS

**Studying the Spectra of Luminous
Infrared Galaxies (LIRGs)**

Lydia Markopouloti

Advisor: Associate Researcher Tanio Diaz Santos - UNIVERSITY OF CRETE

UNIVERSITY OF CRETE
DEPARTMENT OF PHYSICS
M S C T H E S I S

Defended by
Author LYDIA MARKOPOULIOTI

**Studying the Spectra of
Luminous Infrared Galaxies
(LIRGs)**

Date of the defense:
22/02/2022

Acknowledgements

I would like to greatly acknowledge Tanio Diaz-Santos for the perfect guidance he offered and his very supportive and positive attitude throughout this project. I would also like to thank Roman Fernandez Aranda for his help on the programming part of the project. I could not forget to thank Katia Gkimisi and Lee Martin for all the helpful discussions concerning this project.

Contents

1	Introduction	1
2	Data	7
2.1	Data processing	7
2.1.1	CUBISM	7
3	Analysis	13
3.1	Different extraction methods	15
3.1.1	Point-like and Extended sources	15
3.1.2	Physical aperture	16
3.2	Performing the Extractions	18
3.2.1	Create the spectra	19
3.2.2	Stitching the spectra	22
4	Results	27
4.1	Comparison of Spectral Extractions	27
4.2	Stacking	31
4.3	PAH features, emission lines and silicate absorption	38
5	Conclusions	51
6	Appendix	53
	References	57

Contents

1 Introduction

Luminous Infrared Galaxies (LIRGs) are galaxies with infrared luminosities in the range of $10^{11}L_{\odot} \leq L_{IR} < 10^{12}L_{\odot}$ and make up almost 1/3 of the IR sources (Sanders and Mirabel (1996)). LIRGs are not common in the local universe but their number increases significantly (x100) as we move from the current epoch to $z \sim 1$ (Le Floch et al. (2005), Magnelli et al. (2009)). At redshifts of $z \sim 1 - 2$, when the star formation rate (SFR) of the Universe was at its peak, LIRGs dominated the total IR energy density (Caputi et al. (2007)). We can see the dramatic change of the LIRGs contribution as a function of redshift in Figure 1.1. Thus, there must be a strong galaxy evolution which explain these trends. There is also evidence for strong morphological evolution of the LIRG population (Melbourne et al. (2005)). Their morphology could change both as a function of redshift and of IR luminosity. Almost 50% of LIRGs above $z \sim 0.5$ are spiral galaxies, while at lower z the number of spiral galaxies declines. Also, most LIRGs with $L_{IR} \leq 10^{11.5}L_{\odot}$ are non interacting galaxies, while as the luminosity increases, merging galaxies dominate (Hung et al. (2014)).

1. Introduction

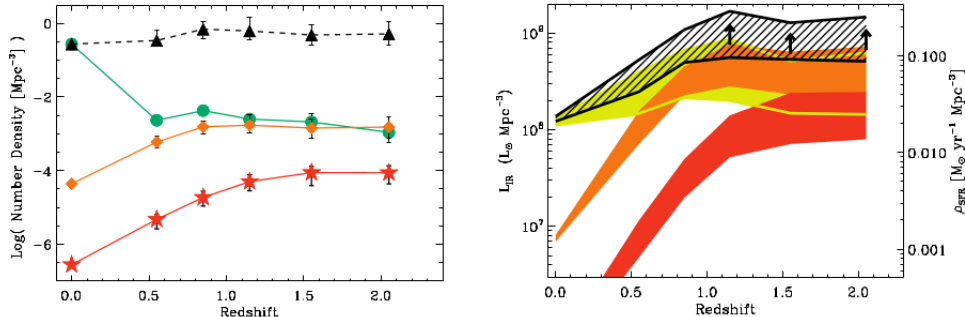


Figure 1.1: The left panel shows the the number density of the galaxies as a function of redshift. Black triangles represent the normal galaxies ($L_{IR} < 10^{11} L_{\odot}$), orange diamonds represent LIRGs, red stars stand for the ULIRGs and the green circles represent the total number of galaxies. The right panel shows the luminosity densities as a function of redshifts. The black hatched area shows the IR luminosity density, the yellow area is the luminosity density of the normal galaxies, the orange area is for the LIRGs and the red area is for ULIRGs. (Magnelli et al. (2011)).

Galaxies form stars, which emit most of their light in the ultraviolet (UV) and optical wavelengths. If the galaxy’s interstellar medium (ISM) is dusty and compact, this energy may be absorbed by this dust and re-emitted in the infrared (IR) as thermal black body radiation (Li and Draine (2001)). That is, IR luminosity is basically reprocessed energy from the UV to the IR by dust particles, which means that we can use IR observations as a tracer of the obscured star formation rate (SFR) in dusty galaxies.

LIRGs are mainly powered by star formation. They contain an underlying stellar population of a few Gyr old, as well as a young ($< 10^7$ years) and massive starburst in their nucleus that dominates the luminosity. In addition, another source of energy is the accretion disk around the central supermassive black hole (SMBH). This and its surrounding structures are called active galactic nuclei (AGN).

In this project, we use observations in the MIR and FIR regime ($\sim 5.2 - 38.4 \mu m$). The MIR spectral region ($3 - 20 \mu m$) is particularly complex. It has strong emission lines that come from highly ionized gas (e.g., $[Ne II]$, $[Ne III]$, $[O IV]$, etc), as well as polycyclic aromatic hydrocarbons (PAH features), and provide us with information about the ISM and the dust properties. There are also absorption bands from silicates which are particularly strong in compact environments with obscured AGN or starburst regions.

The most abundant dust species in the ISM are amorphous silicates (Kemper et al. (2011)), which cause two prominent absorption features at about 9.7 and 18 μm . The 9.7 μm absorption feature is attributed to stretching of the Si-O bonds in silicates. In local LIRGs, there is a tendency for stronger silicate absorption features to be present as the L_{IR} increases (Stierwalt et al. (2013)). This could be a product of a more compact emitting regions in the LIRGs nuclei. Figure 1.2 shows a diagram which presents a comparison between the equivalent width (EW) of the 6.2 μm PAH feature and the strength of the silicate feature (Spoon et al. (2007)). The diagram has been divided in 9 sections (1A to 1C, 2A to 2C, and 3A to 3C). In this diagram different types of galaxies are plotted. The class 1A, is characterized by a featureless hot dust continuum with very weak silicate absorption and PAH lines. As we move to the class 1B, the PAH lines are getting stronger with the hot dust continuum still present. The class 1C is characterized by very strong PAH lines, which dominate the MIR spectral shape, and are representative of star-forming galaxies. Classes 2B, 2C and 2A have stronger silicate absorption features. Class 3A, is characterized by very strong silicate absorption and weak PAH lines, which is a signature of deeply obscured and compact objects, possibly AGN. As we can see, 90% of the galaxies, lay over two branches. The horizontal one (1A, 1B, 1C) which shows the transition between continuum dominated spectra and PAH dominated spectra, and the diagonal one (1C, 2B, 3A) which shows the transition between absorption dominated spectra to PAH dominated spectra. Most local LIRGs are in the 1C class (Stierwalt et al. (2013)) which is characterized by moderate silicate strength and strong PAH features.

1. Introduction

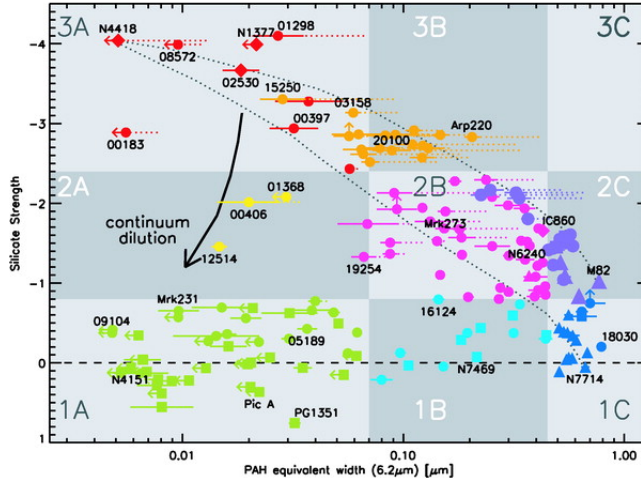


Figure 1.2: Diagnostic plot of the equivalent width of the $6.2 \mu\text{m}$ PAH emission feature vs. the $9.7 \mu\text{m}$ silicate strength. The galaxy spectra are classified into nine classes. From class 1A to 1C, 2A to 2C, 3A to 3B the colors used are green, cyan, dark blue, yellow, pink, purple, red, and orange. Galaxy types are distinguished by their plotting symbol: Filled circles represent ULIRGs and HyLIRGs. Filled triangles represent Starburst galaxies. Filled squares stand for Seyfert galaxies and QSOs. Filled diamonds represent Other infrared galaxies. (Spoon et al. (2007))

LIRGs with high SFR have particularly strong PAH lines which means that PAH features are related to star formation activity (Stierwalt et al. (2013), Díaz-Santos et al. (2010b), Pereira-Santaella et al. (2010)). Some strong PAH feature that appear also in our sample are the 6.2 , 7.7 and $11.3 \mu\text{m}$ PAH emission features. The $11.3 \mu\text{m}$ emission feature appears to be present mostly on a more extended region of the galaxy (Pereira-Santaella et al. (2010)). When compared to the $7.7 \mu\text{m}$ PAH line, the ratio $11.3 \mu\text{m}/7.7 \mu\text{m}$ increases as we go to larger galactocentric distances. Spatially resolved ratios of PAH lines also provide critical information about the ISM properties and the ionization rate of the medium (Díaz-Santos et al. (2010b)).

The Great Observatories All-sky LIRG Survey (GOALS; Armus et al. (2009)) contains 180 LIRGs and 22 ULIRGs. Its aim is to provide a multi-wavelength understanding of the evolution, the formation mechanisms and the chemistry of local LIRGs. In this project we present the extended IR spectra of 55 galaxies in GOALS LIRG systems taken with the low resolution modules (SL and LL) on the Spitzer Infrared Spectrograph (IRS; Houck et al. (2004)). The spectra of the extended emission allows us to

study the properties of the ISM far away from the nucleus of the galaxy. The main goal of this thesis is the comparison of the extended emission spectra with the nuclear emission spectra of LIRGs; that is, with their nuclear starburst. By comparing them, we can investigate the different properties of the ISM as a function of the differences in their SFRs and the AGN contribution.

Studies have shown that the extended emission is an important component of the total emission of galaxies, even in LIRGs, where it is expected that a dominant part of the luminosity arises from their central kiloparsecs. In Figure 1.3 (Díaz-Santos et al. (2010a)), we can see a distribution of the fraction of the extended emission (FEE_λ) for a sample of GOALS galaxies. The fraction of the extended emission, is defined as the extended emission divided by the integrated emission of the galaxy. This histogram shows that 32% of the galaxies in the sample have a median $FEE_\lambda > 0.5$, which means that at least 50% of the MIR emission of these galaxies is extended. The authors also concluded that galaxies tend to be more compact (lower FEE_λ) when they are in their final stage of merger interaction, when there is a significant AGN contribution to the mid-IR wavelengths, and in general, when L_{IR} is above $10^{11.8} L_\odot$ solar luminosities.

In this project we will characterize the spectral properties of such extended component and investigate how they change as a function of a number of integrated galaxy properties.

1. Introduction

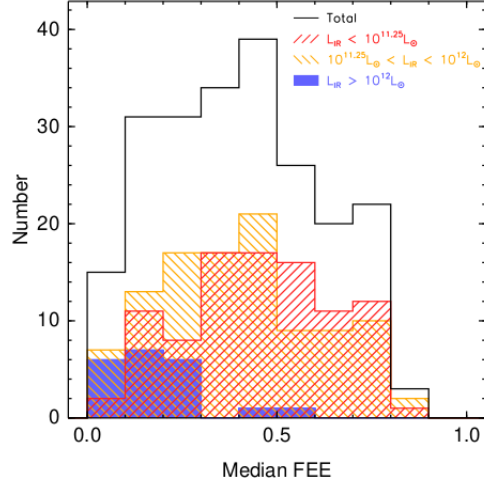


Figure 1.3: Histogram of the median FEE_λ (calculated over the $5 - 15\mu m$ range) for the GOALS sample (black). The red and orange striped, and the blue solid histograms are the distributions of the median FEE_λ for galaxies with $L_{IR} < 10^{11.25} L_\odot$, $10^{11.25} L_\odot \leq L_{IR} < 10^{12} L_\odot$, and $L_{IR} > 10^{12} L_\odot$, respectively. (Díaz-Santos et al. (2010a))

In Section 2 of this project we present the observations as well as the procedure followed to create the spectral cubes used for the analysis. In Section 3 we explain the analysis that we followed for this project, including the different types of spectral extractions. Finally, in Section 4 we present the results of this research and the Future work it could take place.

2 Data

2.1 Data processing

The data used in this project are from the GOALS project (Great Observatories All-Sky LIRG Survey). GOALS contains data of several observatories from X-rays to radio wavelengths, for about 200 LIRGs. In our project, only Spitzer Space Telescope data were used, which covers the spectral regime from 5 to $38\mu\text{m}$. To retrieve the data, the Spitzer Heritage Archive¹ was used. This public archive hosts all the raw, reprocessed and calibrated data from the observations made by the Spitzer telescope.

In order to analyze the extended emission of LIRGs, we downloaded all the spectral mapping observations available for the GOALS sample, obtained with the long-slit, low resolution modules of the Infrared Spectrograph (IRS) instrument. The total number of sources with such kind of data are 55. These observations can be analysed with the CUbe Builder for IRS Spectral Mapping (CUBISM). CUBISM basically builds the spectral cubes out of the grid of long-slit observations. Using basic calibrated data ('BCDs') from IRS maps, we can build 3D spectral cubes, where two dimensions correspond to positions in the plane of the sky, and one dimension is the spectral dispersion. These cubes can be used then for analysis.

2.1.1 CUBISM

In the following, we describe the cube building process in detail. In CUBISM each of our galaxies corresponds to a unique 'Cube Project'. In general, galaxies were observed using the two low resolution IRS modules: Long-Row (LL) and Short-Low (SL). Each

¹<https://sha.ipac.caltech.edu/applications/Spitzer/SHA/>

2. Data

module contains two slits, which will result in an individual cube for each. Therefore, for galaxies with mapping observations in all four low-resolution orders (SL1, SL2, LL1, LL2), four cubes will be built. The SL and LL modules have different pixel scales. The SL modules have pixel scale = $1.85''/\text{pixel}$ while the LL modules have pixel scale = $5.08''/\text{pixel}$. In figures 2.1, 2.2 below, we show a schematic representation of the IRS slits. The wavelengths that each module cover are the following:

- SL2: $5.243 - 7.598\mu\text{m}$
- SL1: $7.534 - 14.737\mu\text{m}$
- LL2: $14.267 - 21.052\mu\text{m}$
- LL1: $20.556 - 38.415\mu\text{m}$

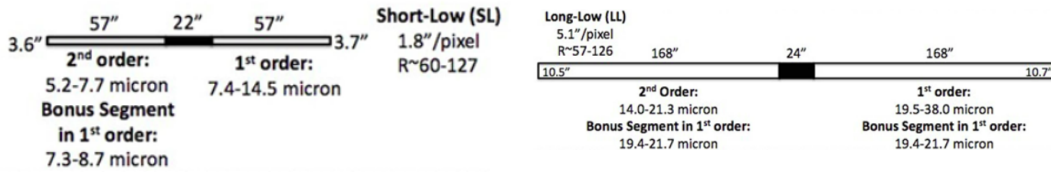


Figure 2.1: SL module characteristics.

Figure 2.2: LL module characteristics.

To process a new cube, we select the data-sets corresponding to the two slits of the same module. The 2D spectral images from where the spectra are extracted contains in some cases strong background emission. To correct for this, the secondary order of the slit can be used as the background of the main order, as each order is dispersed in different parts of the detector. For example, SL2 will be used as the background of SL1 and vice versa. Specifically, to create a background for SL1, all SL2 data should be disabled. Then, from the 'Background' option in the CUBISM environment, we choose 'Set Background from Recs' using Average and Max/Min Trim which trim the unreliable ends of the orders and then calculates the average of the rest reliable background data.

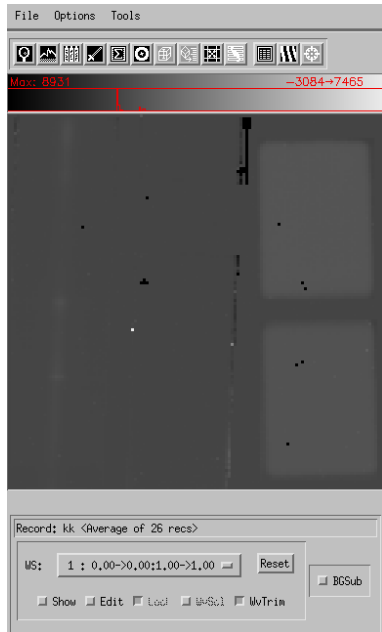


Figure 2.3: Average stack of all the SL1 records in CUBISM environment. On the left we can see a faint vertical white line which is the spectrum of the source. On the upper and lower parts of the image there are some tools of the CUBISM, which were used throughout this process.

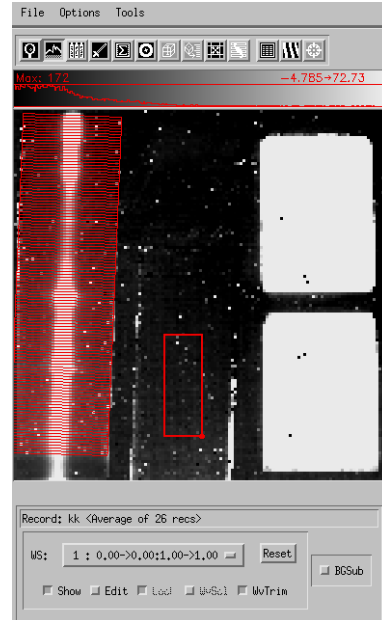


Figure 2.4: Same image as in Figure 2.3 with different highlights. The red, horizontal stripey boxes displays the SL1 slit at each wavelength element. The white vertical source inside the slits is the spectrum of the galaxy. The small red box on the right is used to highlight different features of the image.

Figures 2.3 and 2.4 display the average stack of all the SL1 records in CUBISM environment. In Figure 2.4, the red horizontal rectangles over-plotted over the spectrum (dispersed in the vertical direction) represent each wavelength element of the SL1 order slit. The small red box on the right is used to scale the image based on the histogram of the image. We can use the scaling box to highlight different features of the image, including bad pixels and cosmic rays. In Figure 2.5, both SL1 and SL2 records are displayed: SL1 on the left and SL2 on the right. In Figure 2.6, only SL2 is shown, which is used as the background of SL1.

Once the background data-sets are selected for each order, the final step before building the Cube is to mark the bad pixels. Bad pixels occur in IRS data with a broad range of intensities. If bad pixels are not masked they can degrade the quality of the cubes. Unfortunately CUBISM does not provide an automatic procedure to identify

2. Data

bad pixels, so this task needs to be done manually. Figure 2.7 shows the stacked SL1 records after subtracting the background. Figure 2.8 displays the same image with a different scaling. In the left side of the image, the most intense white dots are manually marked as bad pixels.

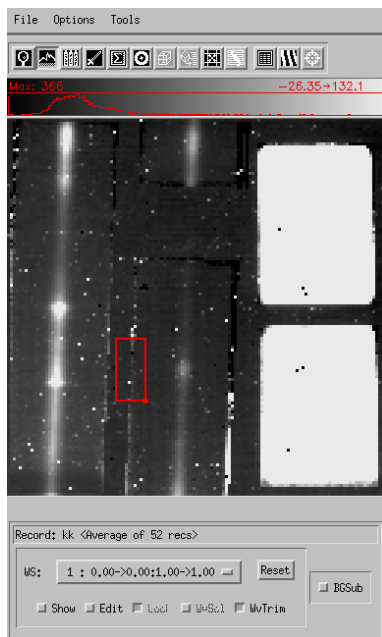


Figure 2.5: Both SL1 and SL2 modules are displayed. The left vertical white line corresponds to the SL1 and the right to the SL2.

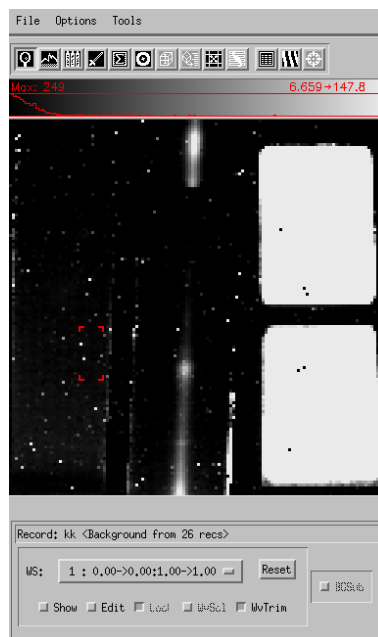


Figure 2.6: Only SL2 module is shown here. This, will be used as the background which will be subtracted from the SL1 cube.

After the cube is built it can be saved in a '.fits' file, which can be further analysed using CUBISM itself or by any other preferred program. Along with the main spectral cube, CUBISM automatically produces an extra associated uncertainty cube, if record-level uncertainties are available. In our project, the rest of the spectral analysis was done with python.

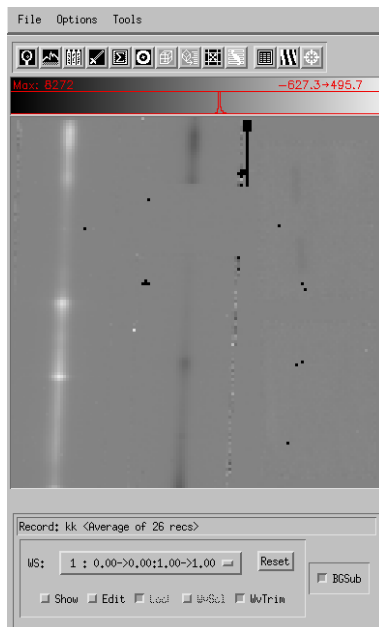


Figure 2.7: Here we display only the SL1 module after we have subtracted the background (Figure 2.6, SL2 module)

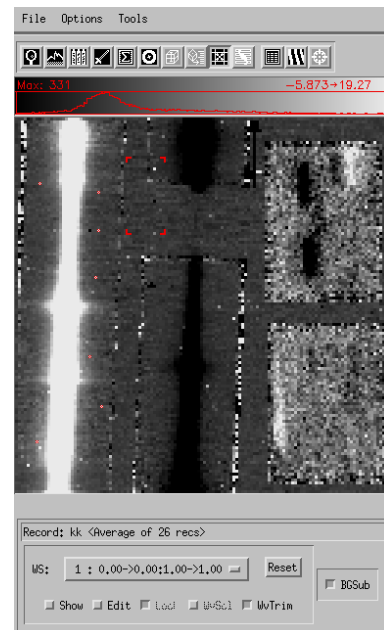


Figure 2.8: Same image as in Figure 2.7 with different scaling. Bad pixels are manually marked (small red crosses next to the histogram scaling box).

2. Data

3 Analysis

In this section we describe the analysis of the data after the cubes have been constructed. For each slice of the cube, the galaxy appears like an image. The source can appear as point source or as an extended source (see Figure 3.1). Depending on the properties we want to take into consideration, four different spectral extractions were conducted.

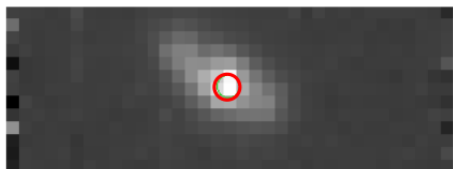


Figure 3.1: SL1 spectral cube of an extended source. The green circle in the middle is the aperture that was used for the nuclear spectrum extraction.

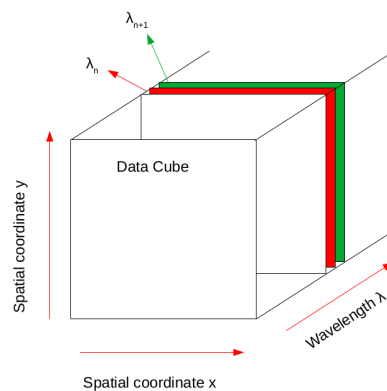


Figure 3.2: Spectral cube diagram. The 3 dimensions of the cube are shown (2 spatial and 1 spectral). Each slice of the cube (red, green), is the image of the galaxy in a different wavelength.

The goal of the analysis is to obtain the spectrum of the source in a nuclear region and in an extended region of the galaxy. For the spectral extraction we will use a circular aperture for the nuclear emission and a circular annulus for the extended emission. As

3. Analysis

we mentioned before, each spectral order will produce an individual cube, covering a short wavelength range (see section 2.1.1). After the extraction is performed in each cube, the spectra will be stitched together and we will have the final spectrum of the galaxy.

We use the tools in the python `specutils` package to manipulate the data cubes. In Figure 3.3 we display representative images of the 4 different cubes associated to the 4 spectral orders.

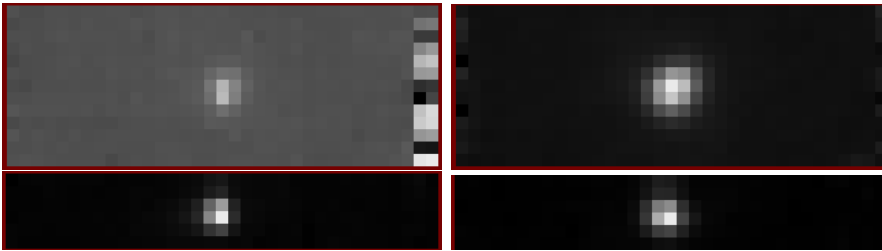


Figure 3.3: Images of the first slice of the cubes in all 4 modules for the galaxy NGC5135. From left to right and top to bottom: SL2, SL1, LL2 and LL1 modules.

First, in order to perform an aperture extraction, the central coordinates of the source need to be found. After exploring multiple methods to find the centroid of the object, we concluded that a 2D Gaussian fitting is the most precise. After the center of the aperture is determined, we measured the flux of the nuclear and the extended emission.

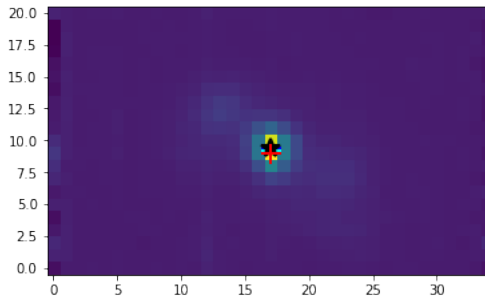


Figure 3.4: Finding the center of the source using various centroid methods for the galaxy IC4734. The red cross is found by using 1D Gaussians to fit the marginal x and y distributions of the data. The light blue cross is found using the center of mass, while the black star is found by calculating the centroid by fitting a 2D Gaussian to the 2D distribution of the data (our preferred method).

3.1 Different extraction methods

3.1.1 Point-like and Extended sources

In this project we extract the nuclear spectra from the cube using 4 different methods. First, we consider the two ideal cases where the observed source is a point-like source or a fully extended source. The angular resolution (full width at half maximum, FWHM) of the Spitzer Space Telescope at $8\mu m$ is $2''$: $FWHM_{8\mu m} = 2''$. We define the radius of the aperture as $r_{ap} = 2 \cdot \sigma$, where $\sigma = FWHM/2.355$. Therefore,

$$r_{ap}^{8\mu m} (") = 2 \cdot \frac{FWHM_{8\mu m}}{2.355} \quad (3.1)$$

For point sources, the wavelength dependence of the angular resolution caused by observations that are diffraction limited should be taken into account. That is, because the Point Spread Function (PSF) increases with wavelength, the flux of a point source will be spread over a larger area. This dependence needs to be taken into consideration because flux will be lost if we use a constant $r_{ap}^{8\mu m}$. The new radius, which will depend on the wavelength, is then:

$$r_{ap,PS}^{\lambda} (") = r_{ap}^{8\mu m} \cdot \frac{\lambda_{module}}{\lambda_{ref}} \quad (3.2)$$

where λ_{module} is the wavelength in question, and $\lambda_{ref} = 8\mu m$ is the reference wavelength at which $r_{ap,PS}^{\lambda} = r_{ap}^{8\mu m}$. We refer to this case as the 2σ extraction for point sources.

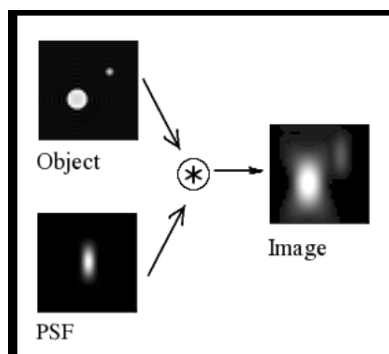


Figure 3.5: Convolution of the real point source with the PSF, gives us the final blurry image

3. Analysis

When an object appears as an extended source and not as a point source (see Figure 3.1), there should not be a dependence between the radius of the aperture and the wavelength because the effect of the PSF is not important. In this case we have the totally fixed radius of the equation 3.1: $r_{ap,ES}^\lambda = 2 \cdot \frac{FWHM_{8\mu m}}{2.355}$, where $FWHM_{8\mu m} = 2''$. We refer to this case as the 2σ extraction with a fixed aperture.

3.1.2 Physical aperture

The previous extraction is defined as an angular scale, and does not take into account the distance to the source, which means that the aperture will cover a different physical size in galaxies that are at different luminosity distances. We can take this under consideration and make the aperture depend on both the wavelength and the distance to the source, so it covers the same physical area in all sources.

In general, any surface at an angular distance d_A with an angular diameter D subtends an angle θ on the sky. This representation is shown in Figure 3.6.

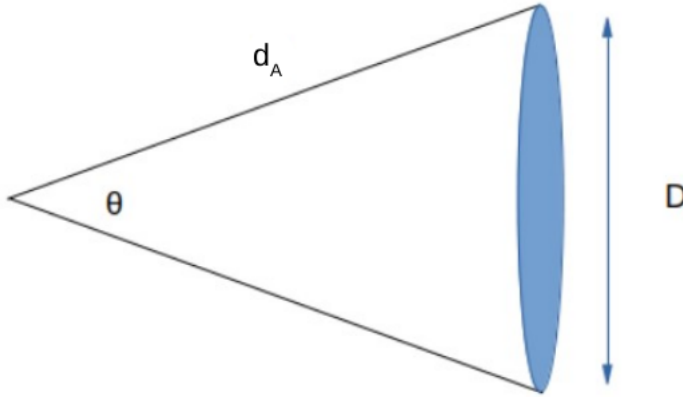


Figure 3.6: The source we observe is represented by the blue ellipse. The diameter of the source is D (kpc), the angular diameter is θ (rad) and d_A (Mpc) is the distance between us and the source.

From geometrical considerations, we know that $d_A = \frac{D}{\theta}$. We also know that $d_A = \frac{d_L}{(1+z)^2}$, where d_L is the luminosity distance of the object (in Mpc) and z is its redshift. So, combining these two relations:

$$\frac{D}{\theta} = \frac{d_L}{(1+z)^2} \Rightarrow D = \frac{d_L \cdot \theta}{(1+z)^2}$$

If θ is expressed in arc-seconds:

$$D = \frac{d_L \cdot \theta('')}{206265 \cdot (1+z)^2} \quad (3.3)$$

We want the physical radius of our aperture to be 1 kpc, thus: $D = 2 \text{ kpc} = 2 \times 10^{-3} \text{ Mpc}$. Also, we set $\theta = 2 \cdot r_{ap}^{8\mu m}('')$. Solving equation 3.3 for these constraints:

$$r_{ap,d_L}^{8\mu m}('') = \frac{10^{-3} \cdot 206265 \cdot (1+z)^2}{d_L} \quad (3.4)$$

From 3.3 we can also calculate at what angular distance, d_A , for which the reference $FWHM_{8\mu m} = 2''$ will equate to a diameter D of 2 kpc: $\frac{d_L}{(1+z)^2} = d_A^{ref} = \frac{10^{-3} \cdot 206265 \cdot 2.355}{2 \cdot FWHM_{8\mu m}} \simeq 121.4 \text{ Mpc}$. If the source is a point-like source, we have both a dependence in wavelength and a dependence in luminosity distance:

$$r_{ap,PS,d_L}^\lambda = r_{ap,d_L}^{8\mu m} \frac{\lambda_{module}}{8\mu m} \quad (3.5)$$

We note that strictly speaking this case is not physically realistic, since if the source is point-like it will appear with the same angular diameter on the sky, independently of its distance. However, this case may be useful for sources that are just slightly resolved, and we include it here to explore all the possible combinations of spectral extractions. We refer to this as the d_L extraction for "point-sources". When an object appears as an extended source and not as a point source and we take under consideration the distance to the object, then the radius will be fixed as the wavelength changes but it will differ from object to object due to their different distances. So, in this case, the aperture radius used for an extended source while accounting for its distance is simply the same as equation 3.4: $r_{ap,ES,d_L}^\lambda = r_{ap,d_L}^{8\mu m}$, and we refer to this case as the d_L extraction with a fixed aperture.

3. Analysis

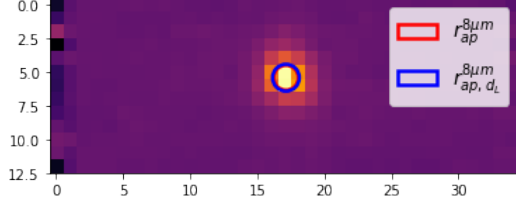


Figure 3.7: Example of the aperture sizes at the reference wavelength $\lambda_{ref} = 8\mu m$. The red aperture has radius= $r_{ap}^{8\mu m}$ and the blue aperture has radius= $r_{ap, d_L}^{8\mu m}$. The galaxy is $M+0-29-23$, which is at a distance $d_L = 117Mpc$. The two apertures are almost the same because the distance of the source is very close to the reference distance $d_L = 121Mpc$ (see previous section).

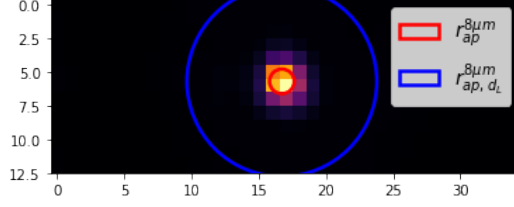


Figure 3.8: Same as Figure 3.7 but for the galaxy NGC1068 which is at a distance $d_L = 15.9Mpc$. We can see that the blue aperture is much larger than the red one due to the source being much closer than the reference distance $d_L = 121Mpc$.

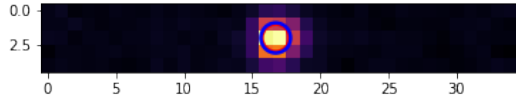


Figure 3.9: Example of the aperture sizes at wavelength $\lambda = 24\mu m$ (LL1 module) for the galaxy $M+0-29-23$. The red aperture has radius= $r_{ap, PS}^{24\mu m}$ and the blue aperture has radius= $r_{ap, PS, d_L}^{24\mu m}$. At this wavelength, the apertures have been increased by a factor $\frac{\lambda=24\mu m}{\lambda_{ref}} = 3$. Due to the different pixel scales of the modules SL ($1.85''/\text{pixel}$) and LL ($5.08''/\text{pixel}$), this factor of 3 is not obvious.

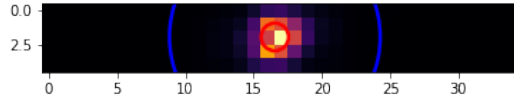


Figure 3.10: Same as Figure 3.9 but for the galaxy NGC 1068. The image is at $24\mu m$ and we can see how much bigger is the blue aperture from the red due to the small d_L .

3.2 Performing the Extractions

In the following we briefly explain each step in the implementation of these extractions, which have been carried out using python scripts and codes developed specifically for this project.

3.2.1 Create the spectra

The analysis starts by reading the fits files and a file containing the redshift and the distance luminosity of each source. Every time that we run the code, it analyses only one cube per time (SL1, SL2, LL1, LL2) for every source. In this phase, our goal is to calculate the flux of the nuclear emission. To do so, we will use a circular aperture centered around the source (using the 2D Gaussian centroid method described above). Then, the radius of the aperture is calculated based on the 4 different ways we explained before. That is, using an aperture that depends or not on the wavelength (point source versus extended source) and on the luminosity distance (angular size versus physical size). To calculate the flux at each wavelength, we simply sum over the pixels inside the aperture.

For the uncertainty of the flux, we use the uncertainty cubes that were also built with CUBISM. Again, the same radius is used, we take the same circular aperture and we use the relation: $N = \sqrt{\sum n_i^2}$. Where N is the uncertainty of the total flux in the aperture and n_i is the uncertainty of the pixel i within the aperture, which is evaluated in the uncertainty cube. We do that for all the wavelengths of the cube separately.

To measure the extended emission we use a circular annulus. Independently of the 4 different cases of nuclear extraction, we use a fixed radius for the annulus which we define as:

$$r_{ann}^{ext.in} = r_{ap}^{ref} \cdot 4.5 \quad (3.6)$$

$$r_{ann}^{ext.out} = r_{ann}^{ext.in} \cdot 1.3 \quad (3.7)$$

where, $r_{ann}^{ext.in}$ is the inner radius of the annulus, which is defined as 4.5 times the reference radius, r_{ap}^{ref} , that was used to calculate the nuclear flux (at $\lambda_{ref} = 8\mu m$). The factor 4.5 was derived practically, in order for the annulus to be sufficiently separated from the nuclear aperture. In other words, the radius of the nuclear aperture may have a linear dependence with the wavelength. In that case the relative growth of the nuclear radius could be approximated as $\frac{\lambda_{final}}{\lambda_{ref}} \simeq \frac{38}{8} \simeq 4.5$. That is, the nuclear radius will grow 4.5 times when it reaches the final wavelength of the LL module, with respect to the radius at $8\mu m$.

3. Analysis

The $rad_{ann}^{ext\ out}$ is the outer radius of the annulus and it is arbitrarily defined as the inside radius of the annulus times 1.3. It is important to note one more time that for the extended emission we keep the annulus radii fixed as a function of wavelength. This is because our goal is to find the properties of the extended emission of the galaxy on a fixed extended region. If the radius was changed with wavelength, the results would not be representative of the same physical region around the galaxy.

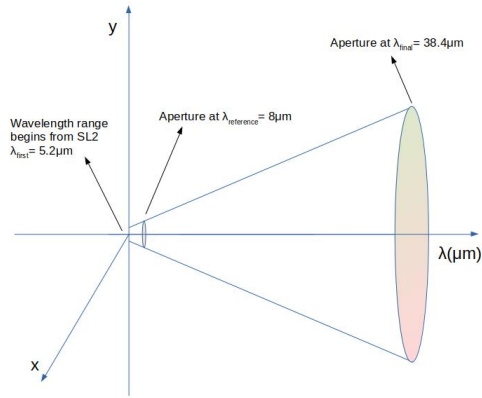


Figure 3.11: Schematic representation of the growing aperture with wavelength. The wavelength range begins from the module SL2 at $\lambda_{first} = 5.2\mu m$ and ends at the module LL1 at $\lambda_{final} = 38.4\mu m$. The first small aperture at $\lambda_{ref} = 8\mu m$ is the reference aperture. The rest of the apertures are following the $\frac{\lambda_i}{\lambda_{ref}}$ relation.

The flux density for the extended emission is calculated using the circular annulus and taking the median of the flux inside the annulus. That is, at each wavelength, in a specific and fixed annulus, we find the median value of the flux. For the uncertainty of the extended emission flux we take the same annulus as before but we use the uncertainty cube. To be conservative we calculate the median value of the uncertainties

inside the annulus (the uncertainty of the distribution rather than the uncertainty of the mean). We do that for all the wavelengths inside the uncertainty cube separately.

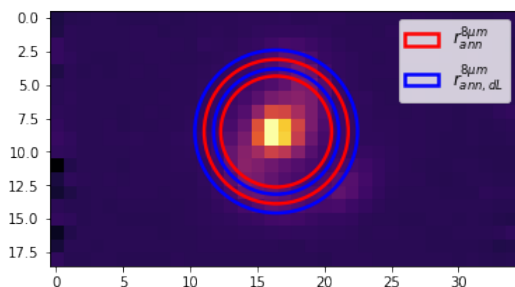


Figure 3.12: Example of the annuli (at $\lambda_{ref} = 8\mu m$) used for measuring the extended emission. The red aperture has $r_{ann}^{ext.in} = r_{ap}^{8\mu m} \cdot 4.5$ and the blue aperture has $r_{ann}^{ext.in} = r_{ap, dL}^{8\mu m} \cdot 4.5$. The galaxy shown is NGC6786, which is at a distance $d_L = 113Mpc$ (relatively close to the reference distance $d_L = 121Mpc$). The annuli are very similar because the distance of the galaxy is very close to our reference distance.

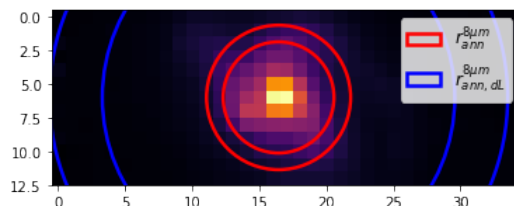


Figure 3.13: Same as Figure 3.12 but for the galaxy NGC3256 which is at a distance $d_L = 38.9Mpc$. The blue annulus is much bigger than the red one because the galaxy is very close to us.

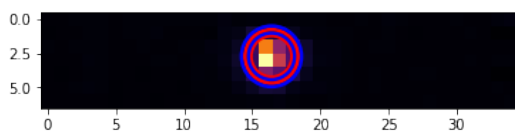


Figure 3.14: Example of the extended emission annuli for the galaxy NGC6786 (Figure 3.13) at a wavelength $\lambda = 24\mu m$. The radii are the same as the ones on Figure 3.13 (same in arcseconds for the red one, same in kpc for the blue one). The pixel scales between the modules are different and this is why here they look smaller.

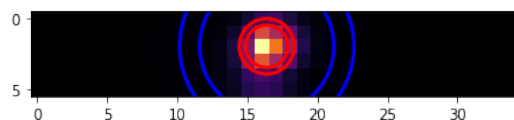


Figure 3.15: Same as Figure 3.14 for the galaxy NGC3256 (Figure 3.12)

We note that before calculating the fluxes, we subtracted any background emission (if present) by estimating a background mean flux density using an annulus with radii:

$$rad_{bkg.in} = rad_{ref} \cdot 10$$

3. Analysis

$$rad_{bkg.out} = rad_{bkg.in} \cdot 1.3$$

After following these steps for every source we have, for each type of extraction, 4 different spectra of the nuclear emission, 4 different spectra of the extended emission, and 4 more different spectra of the background emission, each one corresponding to the 4 different orders (SL2, SL1, LL2, LL1; in increasing wavelength). The final step is to stitch these 4 spectra into one for each source, in order to have a single spectrum for all the wavelengths between SL2 and LL1.

3.2.2 Stitching the spectra

If we display all the spectra into one, we will notice that the mean value of the flux changes from module to module. We should do a scaling in order for the final spectrum to be useful and continuous. The scaling is made according to module LL1 which has the highest mean flux. We scale the rest of the modules to LL1. First, we scale the SL2 module to the SL1. In general, neighborhood modules (SL2 and SL1; SL1 and LL2; LL2 and LL1) have overlapping wavelength regions:

- SL2-SL1: $7.534 - 7.598\mu m$
- SL1-LL2: $14.267 - 14.737\mu m$
- LL2-LL1: $20.556 - 21.052\mu m$

These overlapping regions are used for the stitching, and we calculate the scaling factors as:

$$\text{factorSL2SL1} = \frac{\text{medianSL1}}{\text{medianSL2}}$$

Multiplying the SL2 spectrum by factorSL2SL1 we successfully scale SL2 to SL1. Next:

$$\text{factorSL1LL2} = \frac{\text{medianLL2}}{\text{medianSL1}}$$

Now, multiplying the previous spectrum by factorSL1LL2 we successfully scale SL1 and SL2 to LL2. Finally we do the same to scale to LL1:

$$\text{factorLL2LL1} = \frac{\text{medianLL1}}{\text{medianLL2}}$$

In this way we scale up all the modules to LL1. In Figures 3.16, 3.17, 3.18 we display some examples of this process. The x-axis shows the wavelength range, where we should notice that it contains the entire wavelength range of all modules (SL2,SL1,LL2,LL1). The y-axis shows the flux of the nuclear (Figures 3.16, 3.17) or the extended emission (Figure 3.18). The red line represents the final scaled spectrum while the gray line shows the pre-scaled spectra. Figure 3.16 shows the nuclear emission spectrum extracted with a fixed aperture. We can see that the flux of the modules SL2 and SL1 was larger than the flux of LL2 and LL1 modules before the scaling. This happens because the aperture remains fixed throughout all the wavelengths while the pixel scale between the modules changes. That is, even though the aperture is fixed in angular size ($2''$), the size of the pixel changes (SL: $1.85''/\text{pixel}$, LL: $5.08''/\text{pixel}$). Thus, the aperture corresponding to the LL will be 2.78 times smaller (in pixels) than that of the SL module. That means that the flux inside the aperture will be less precise because the aperture sum is done over an area with radius of ~ 1 pixel or less.

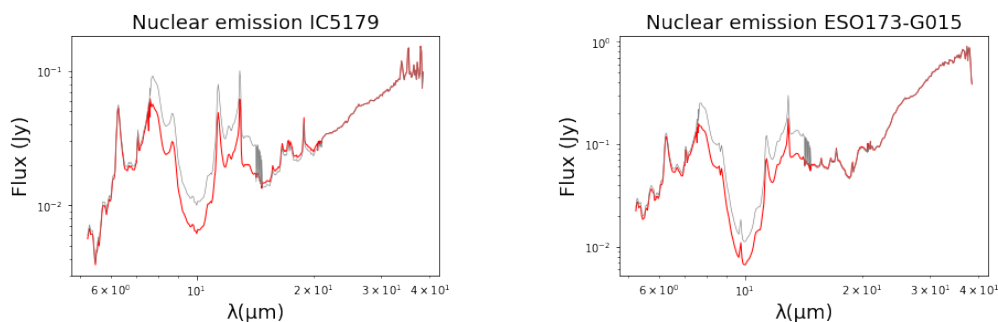


Figure 3.16: Stitching and scaling the nuclear emission spectra extracted with a fixed aperture of $2''$ (no distance dependency). Two galaxies are shown as examples: IC5179 and ESO173-G015 left and right, respectively. The faint gray line shows the pre-scaled spectra while the red line shows the final spectra after the stitching and the scaling process. The gray spectrum shows that the flux on the modules SL2 and SL1 was larger than that of longer wavelengths. This happens because, despite the fact that the slit of LL modules is bigger than the slit of SL modules, the aperture for the extraction is smaller on the LL modules because of the pixel scale. Then, pixelation effects combined with the loss of flux due the fixed aperture make the SL fluxes to be larger than LL fluxes.

In figure 3.17 we show the nuclear emission spectrum for the same galaxies as in figure 3.16, but here a wavelength dependent aperture is used. The size of the aperture increases as we increase the wavelength (by a factor of $\frac{\lambda_i}{\lambda_{ref}}$). We can see that here

3. Analysis

the gray spectrum is almost the same as the red spectrum, which means that the fluxes between the modules were almost the same without any scaling. This can be explained as now the aperture is growing as a function of the wavelength. So, at longer wavelengths (LL) the aperture will be larger in " and thus, even though there is still the same difference regarding the pixel scale as before, the pixelation effect is less significant.

Finally, Figure 3.18 displays the extended emission spectrum of two example galaxies. We can see that before the scaling, the flux of the SL2 and SL1 modules is slightly smaller than that of LL2 and LL1. In this case, because the annuli are sufficiently big, there are no important pixelation effects and thus the flux is approximately the same in all the modules.

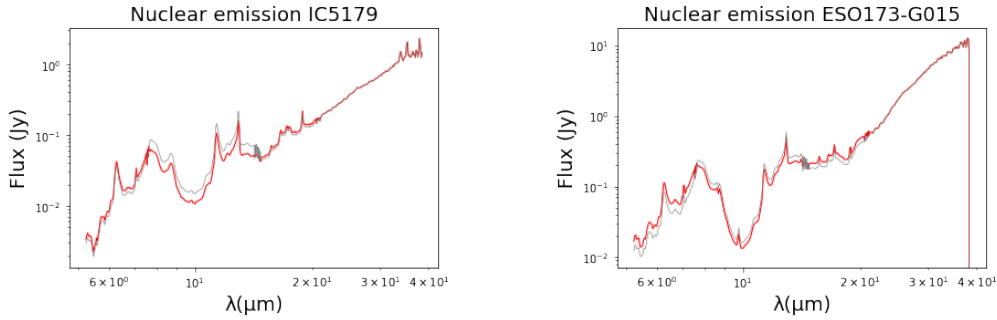


Figure 3.17: Same as Figure 3.16 but here the aperture was wavelength dependent. In this case, the gray line shows that the flux on the modules SL2 and SL1 is almost the same with the flux of LL2 and LL1 Modules. This is happening because despite the smaller aperture of the LL modules because of the pixel scaling, there is the growth of the aperture by a factor of λ_i/λ_{ref} , so the differences between the modules are less significant.

Summarizing, after the scaling process, we have obtained the continuous spectra extracted with the different apertures for every galaxy.

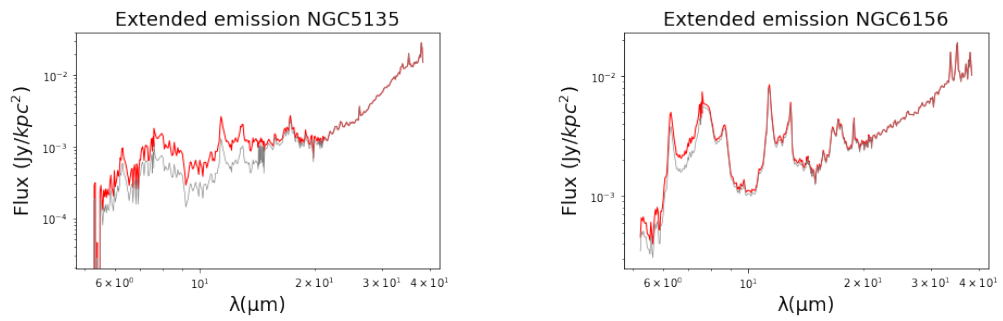


Figure 3.18: Same as in figures 3.16, 3.17 but for the extended emission using an annulus based on distance dependency. These spectra are for the galaxies NGC5135 and NGC6156. The gray line shows that the flux on the modules SL2 and SL1 was smaller than that at longer wavelengths.

3. Analysis

4 Results

4.1 Comparison of Spectral Extractions

Now that all the spectra have been constructed, we can compare them and investigate the differences. In Figures 4.1, 4.2, 4.3, in the left panel in the upper row we show a comparison of the 4 different spectra for the nuclear emission, and in the right panel the two different spectra for the extended emission. For the nuclear spectra, the black spectrum represents the point source spectral extraction, where there is also the distance dependence (r_{PS,d_L}). The red spectrum represents the aperture which is fixed as the wavelength changes but depends on the distance of the source (r_{ES,d_L}). The green spectrum shows the aperture that only depends on the wavelength, but not on the distance of the source ($r_{PS,2\sigma}$). Lastly, the blue spectrum stands for the aperture that is fixed and does not depend on the distance of the source either ($r_{ES,2\sigma}$). The right panel in the upper row displays the extended emission spectra for only 2 cases (with and without a dependence on luminosity distance) as the radii of the annulus does not depend on wavelength.

In the bottom panel of the figures 4.1, 4.2, 4.3 we present the images of the nuclear apertures as well as the annuli we used for the extraction of the nuclear and the extended emission, respectively. All of them are shown at the reference wavelength $\lambda_{ref} = 8\mu m$.

In Figure 4.1 the spectra of the galaxy NGC2388 are displayed. This source is at a $d_L = 62.1Mpc$ (almost at half of our reference distance $d_L = 121Mpc$). In the first plot, we can see that the spectrum pairs: red and black, and then green and blue, have similar fluxes at the lowest wavelengths and also converge at $\lambda_{ref} = 8\mu m$. The red and black spectra, which correspond to the distance dependent cases, have larger fluxes and

4. Results

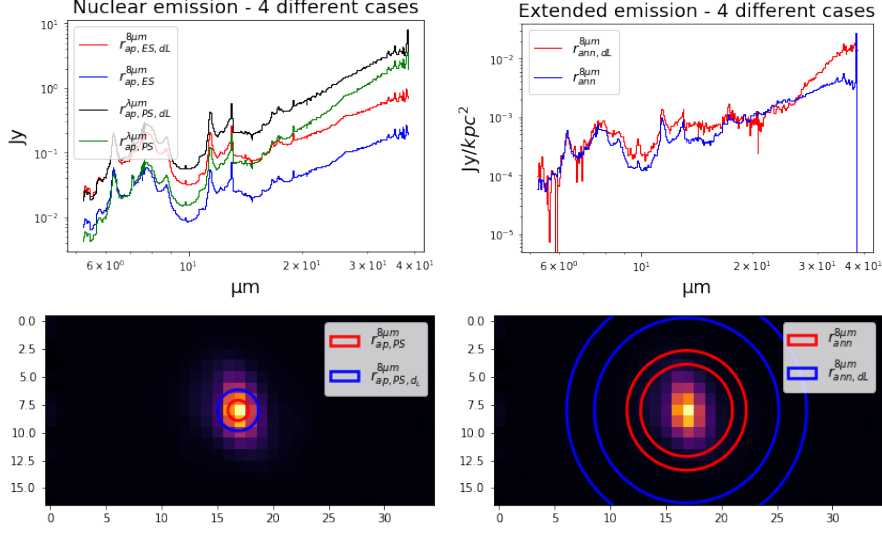


Figure 4.1: In the upper row, the left plot shows the 4 different spectra of the nuclear emission. Black spectrum corresponds to $r_{PS,dL}$, the green spectrum to $r_{PS,2\sigma}$, the red spectrum to $r_{ES,dL}$ and the blue spectrum corresponds to $r_{ES,2\sigma}$. The right plot shows the extended emission spectra where red spectrum corresponds to the distance dependent cases while the blue spectrum corresponds to the 2σ cases. Below, there is image of the nuclear apertures (on the left) and the extended emission annuli (on the right). The blue color stands for the distance dependent aperture and the red for the wavelength dependent aperture. Both of the images in the bottom panel are at the reference wavelength $\lambda_{ref} = 8\mu m$. The galaxy is the NGC2388 is at a $d_L = 62.1 Mpc$.

this is expected as these apertures are larger than for the 2σ case. This is clearly shown by the visual representation of the nuclear apertures (first panel on the bottom row). We can also see that the pair of spectra black and green, have an almost same growth at the beginning. At longer wavelength though, the green spectrum rises faster. This is because as the 2σ aperture grows with the wavelength we include more and more flux from the source (which is close to a point source) and thus the green spectrum has a sudden increase. In the d_L extraction, the aperture is already big enough at all wavelengths and thus there is no significant flux gain because of the bigger aperture. The pair of the spectra red and blue look similar throughout all wavelength range. In other words the ratio between the spectra stays almost the same.

In the upper right panel of the figure 4.1, which shows the extended spectra of the galaxy, we can see that the red spectrum, which corresponds to the physical dependent

case, is much smoother than the blue spectrum. All the PAH lines and the emission features are very weak and this is expected as the annulus with radius $r_{ann}^{ext. in}$, corresponds to a larger physical radius (because the source is relatively close to us). This can be seen on the bottom right panel. The blue annulus is big enough and the extended flux that we measure contains less emission associated to the nuclear region.

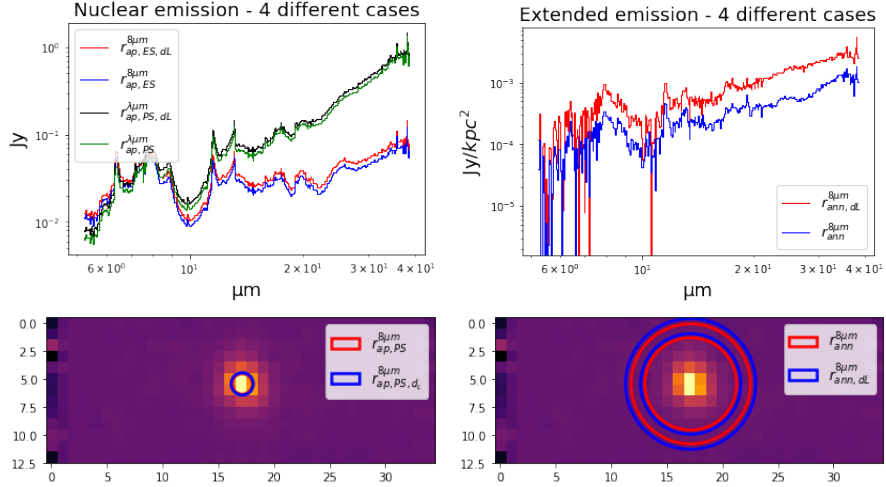


Figure 4.2: Same as in Figure 4.1 but for the galaxy M+029-23. This galaxy is at a $d_L = 117Mpc$, a distance very close to our reference distance $d_L = 121Mpc$. We can see that the green and black spectra in the left plot on the upper panel look very similar and have almost the same shape.

In Figure 4.2, the spectra of the galaxy M+0-29-23 are displayed. This galaxy is at a distance $d_L = 117Mpc$, which is close to our reference distance $d_L = 121Mpc$. This, implies that the $r_{PS,2\sigma}$, r_{PS,d_L} and $r_{ES,2\sigma}$, r_{ES,d_L} will be very close and so their nuclear spectra will be similar. This is something we can see in the left panel of the figure. The black, green spectra and the red, blue spectra are very close to each other throughout the whole wavelength range. The extended emission spectra in the right panel are also very similar.

4. Results

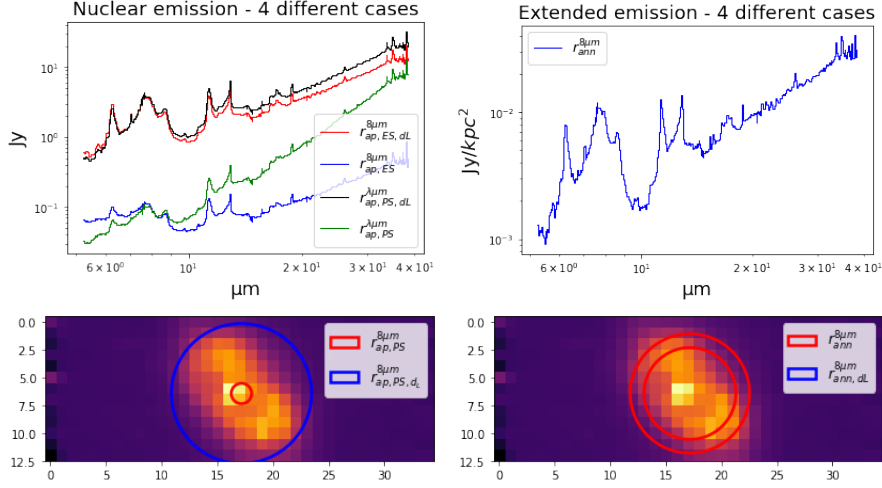


Figure 4.3: Same as in Figure 4.1 but for the galaxy NGC1365. This galaxy is at a $d_L = 17.9 Mpc$, a distance very close to us. We can see that the black and green spectra in the upper left plot, have much higher flux than the other two and this is expected as the d_L aperture is much larger than the 2σ . In the upper right plot, there is only one spectrum, corresponding to the 2σ extraction. We could not measure the extended emission for the d_L extraction, because the aperture is bigger than the cube.

Finally, we show a third case in Figure 4.3, which displays the spectra of the galaxy NGC1365. This source is at a very close distance $d_L = 17.9 Mpc$. This implies that the distance dependent apertures will be much larger than the others, which we can see in the visual representation below. The spectra of the distance dependent cases (red and black) are much larger than the other two spectra. The green spectrum corresponds to the wavelength dependent case, where for an extended source, the flux rapidly increases as the aperture grows with wavelength. The blue spectrum stays very low in all the wavelength range. The PAH lines and the absorption features of the green and blue spectra seem to be very weak in comparison with the black and red spectra respectively. This probably implies that there is star formation activity in the extended region of the galaxy that causes this difference. The right panel shows the extended emission spectra of the galaxy, which is only one. We cannot measure the extended emission in the distance dependent case, as the inner radius of the annulus (that corresponds to the distance dependent nuclear $r_{ap} = 1 kpc$ aperture) falls outside of the cube.

4.2 Stacking

After extracting the whole spectra of the nuclear and the extended emission for all the sources, we can stack them as a function of some galaxy properties. For example we could stack the spectra as a function of the Active Galactic Nuclei (AGN) fraction of the galaxies. The spectra that correspond to galaxies with higher AGN fraction will weight more than those with a small AGN fraction. The properties that we took under consideration for this weighting are the AGN fraction, the infrared luminosity (L_{IR}), the star formation ratio (SFR), the stellar mass of the galaxy and the merger stage. We stack the spectra for the nuclear and extended emission, where the nuclear extraction has been performed using the 2σ , wavelength dependent method.

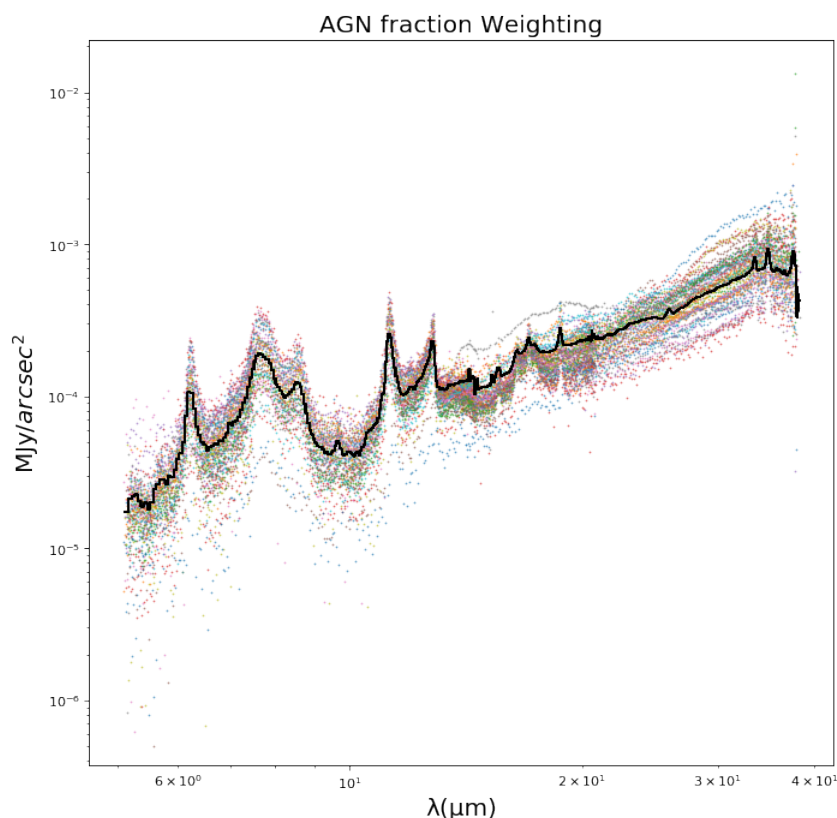


Figure 4.4: Stacking as a function of the AGN fraction. The x axis is the wavelength in logarithmic scale, and in y axis, there is the Flux of the extended emission. The dots represent the different extended spectra of all the sources. The different colours of the dots stand for the different sources. The black line represents the stacked, weighted spectrum.

4. Results

In Figure 4.4, we can see the stacking as a function of the AGN fraction. The extended emission spectra of all the individual galaxies in our sample are displayed with little dots in different colors. The black continuous spectrum is the stacked spectrum weighted as a function of the AGN fraction. Figures 4.5, 4.6 show the different weighting methods and how they affect the stacked final spectrum (either for the extended emission or for the nuclear emission). The different line colours represent the different weighting properties. The red spectrum stands for the AGN fraction weighting, the green spectrum for the SFR weighting, the blue spectrum for the L_{IR} weighting, the grey spectrum for the stellar mass weighting, and the black spectrum corresponds to the stacked spectra without any weighting. We can see that the AGN weighted spectrum (red line) has weaker PAH fluxes and shallower silicate absorption than all the other stacked spectra. This can be explained if we consider the presence of the hot dust continuum because of the higher AGN fraction. In the nuclear emission, we can see that the effect of this contribution due to the hot dust continuum is stronger because we extracted the spectra on the AGN itself.

The blue and the green spectra correspond to the weighting according to the infrared luminosity and the SFR respectively. We can see that these two stacked spectra are very similar both for the nuclear and the extended emission. This is something we would expect as the SFR of the galaxy is closely related to its L_{IR} . For both the nuclear and the extended emission, the silicate absorption of the blue and green spectra seems to be slightly deeper. This was anticipated as there is a tendency for deeper silicate features in local LIRGs with increasing L_{IR} , especially for the most luminous LIRGs (Stierwalt et al. (2013)). This could be related to the presence of more compact emitting regions in the LIRGs nuclei.

The next figures (4.6 to 4.10) show the spectra of galaxies according to their properties in different bins. The histogram shows the distribution of the galaxies according to the property (the bins in all histograms have equal-width in the given property range). In each figure the two lower panels show the stacked spectrum of the extended and nuclear emission for each bin of the histogram. These plots will help us identify how and to what extent some galaxy properties affect their MIR spectrum.

In Figure 4.6 the galaxies are classified according to their infrared luminosity. The first bin of the histogram represents the galaxies with lower $L_{IR} < 1.6 \times 10^{11} L_{\odot}$ and 23 galaxies are falling into this category. In the second bin, there are also 23 galaxies

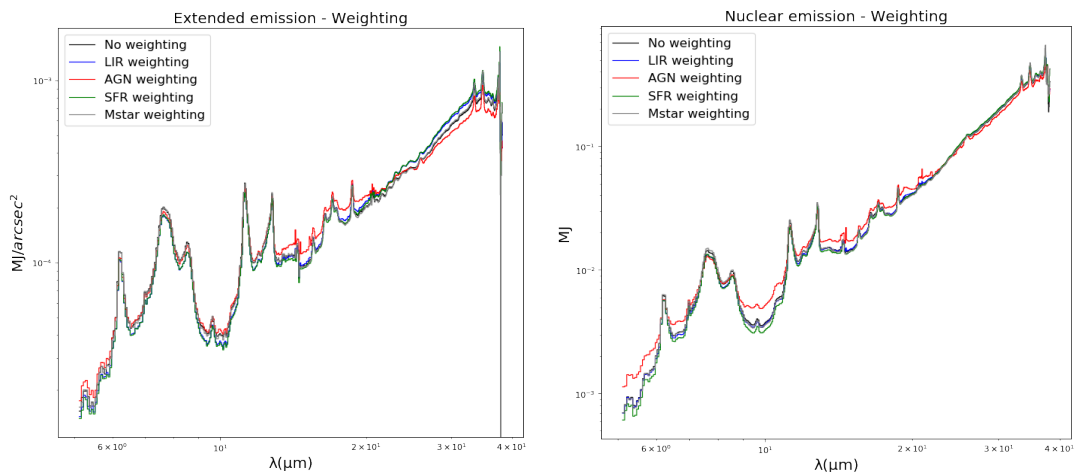


Figure 4.5: Stacked spectra for the different weighting mechanisms. The left figure is for the extended emission while the right figure is for the nuclear emission. The red spectrum color corresponds to the weighting according to the AGN fraction, the blue spectrum to the LIR, the green to the SFR, the grey to the Mass of the galaxy and the black color corresponds to the stacked spectra without any weighting.

and the luminosities extend up to $3.2 \times 10^{11} L_{\odot}$. Finally, the third bin contains the 6 galaxies with the highest luminosities (up to $4.7 \times 10^{11} L_{\odot}$). In the lower panels, the black spectrum represents the galaxies with the lowest infrared luminosities, the blue spectrum are the LIRGs with intermediate luminosities, and the red spectrum are the most luminous galaxies in the sample. We can see that in both the extended and the nuclear emission the red spectrum seems to correspond to weaker PAH lines and deeper silicate absorption.

In Figure 4.7 the galaxies are classified according to their AGN fraction. The data were separated into 2 bins. The first bin of the histogram represent the galaxies with lower AGN fraction $AGN\ fraction < 0.5$ while the second bin contains only 2 galaxies where the AGN fraction goes up to 1. This uneven classification into these 2 bins is very effective, as it gives us more robust results in how a high AGN fraction affect the spectrum of a galaxy in nuclear and extended regions. The black spectrum represents the first bin and the blue spectrum the second bin. It is clear that when the AGN fraction dominates (more than 50%), the spectrum is different. The hot dust continuum from the AGN suppresses the PAH features and the silicate absorption. The galaxies that exhibit the black nuclear spectrum could be classified in the class

4. Results

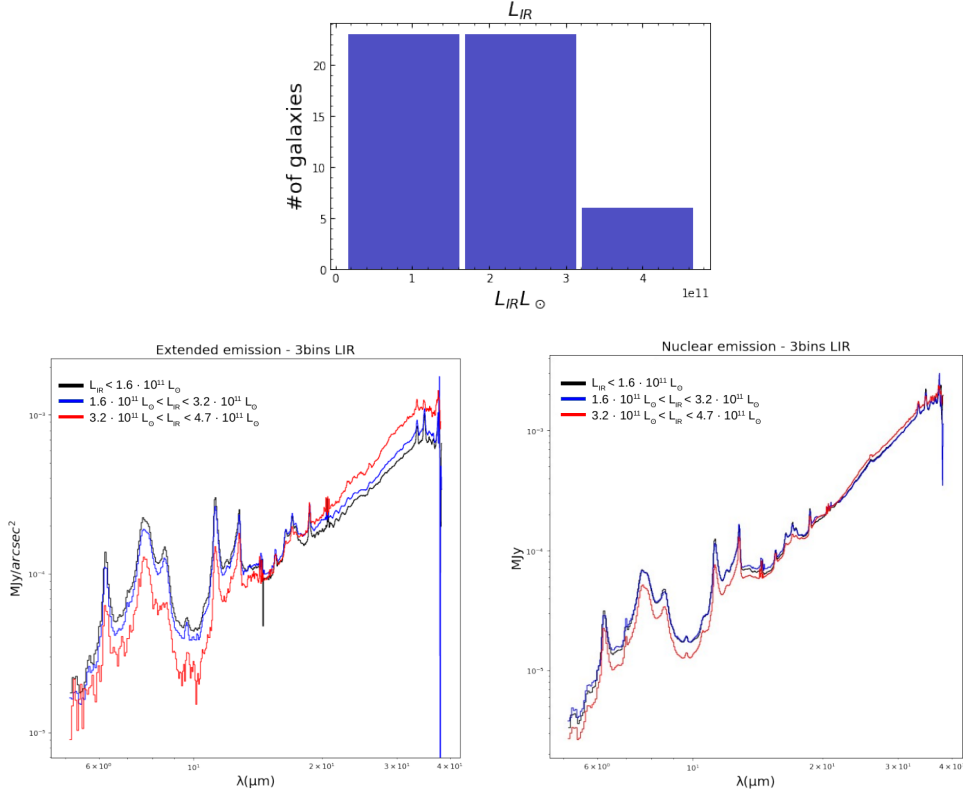


Figure 4.6: The galaxies of our sample are classified into 3 bins according to their L_{IR} . The two plots below the histogram, show the stacked spectra for the extended and the nuclear emission. The black spectrum correspond to the first bin of the histogram, the blue spectrum to the second bin and the red spectrum to the third bin of the histogram. The axis of the plots are logarithmic. The x axis is the wavelength in μm and the y axis is the flux of the emission.

1A in Spoon et al. (2007) diagram (see Figure 1.2). Particularly, strong AGN with no significant obscuration produce nearly featureless spectra, almost entirely coming from the hot dust emission. This effect is much stronger on the nuclear emission, as the AGN contribution in this region is much more dominant. The left plot for the extended emission is particularly interesting. We can see that both black and blue spectra have almost the same PAH lines until $\lambda = 14\mu\text{m}$. At longer wavelengths, the blue spectrum for the highest AGN fractions changes. It becomes featureless, almost like a hot dust continuum. This could tentatively indicate that the AGN may be able to heat the medium even in the extended regions of the galaxy.

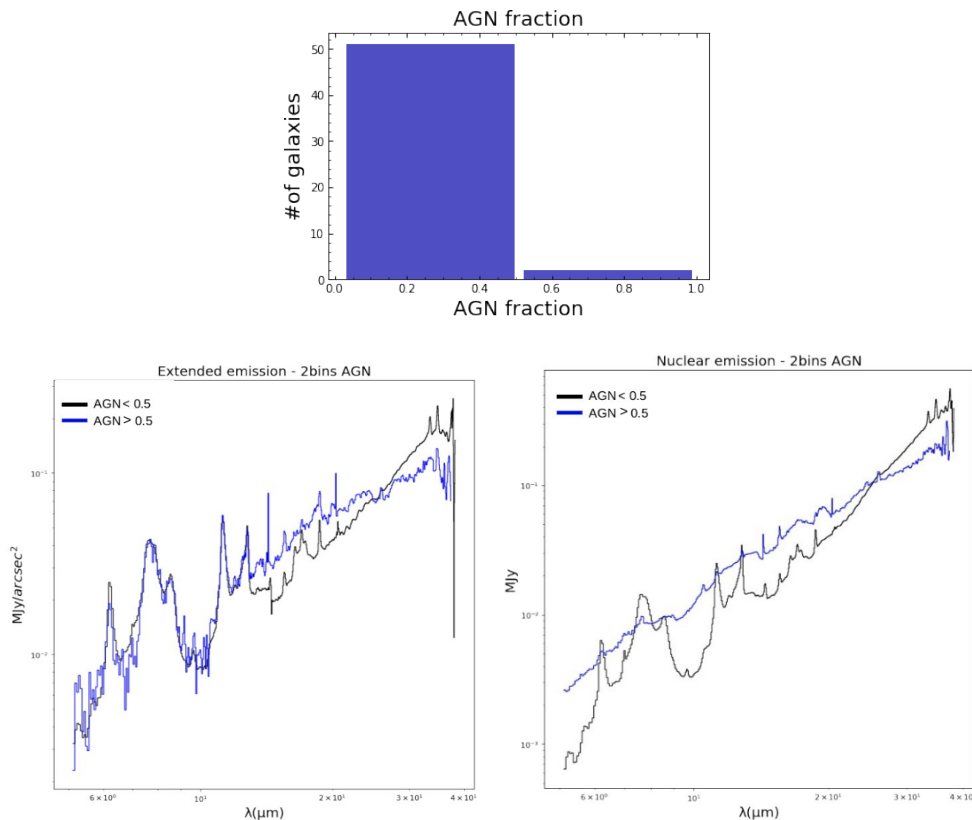


Figure 4.7: Same as in Figure 4.6 but the property taken under consideration is the AGN rate of the galaxies. High AGN fraction leads to a more smoothed spectrum, with weak absorption and emission features spectrum, particularly for the nuclear emission. This is more prominent on the nuclear emission spectra. On the extended emission spectra we can see that the blue spectrum shows a different behavior after $\sim 1\mu\text{m}$ which indicates that the medium in the extended regions is heated by the AGN.

In Figure 4.8 the galaxies are binned according to their stellar mass. The data were separated into 3 bins. The first bin contains 21 galaxies with stellar mass $< 9.6 \times 10^{10} M_{\odot}$, the second bin contains 26 galaxies with masses that extend up to $1.8 \times 10^{11} M_{\odot}$ and third bin contains 8 galaxies with the highest masses, up to $2.6 \times 10^{11} M_{\odot}$. The plots with the stacked spectra of the extended emission show that all the spectra are very similar to each other, exhibiting similar PAH features and silicate absorption.

In the Figure 4.9, the galaxies are distributed according to their merger stage. The merger stage of a galaxy represents to which extent a galaxy merger has been completed.

4. Results

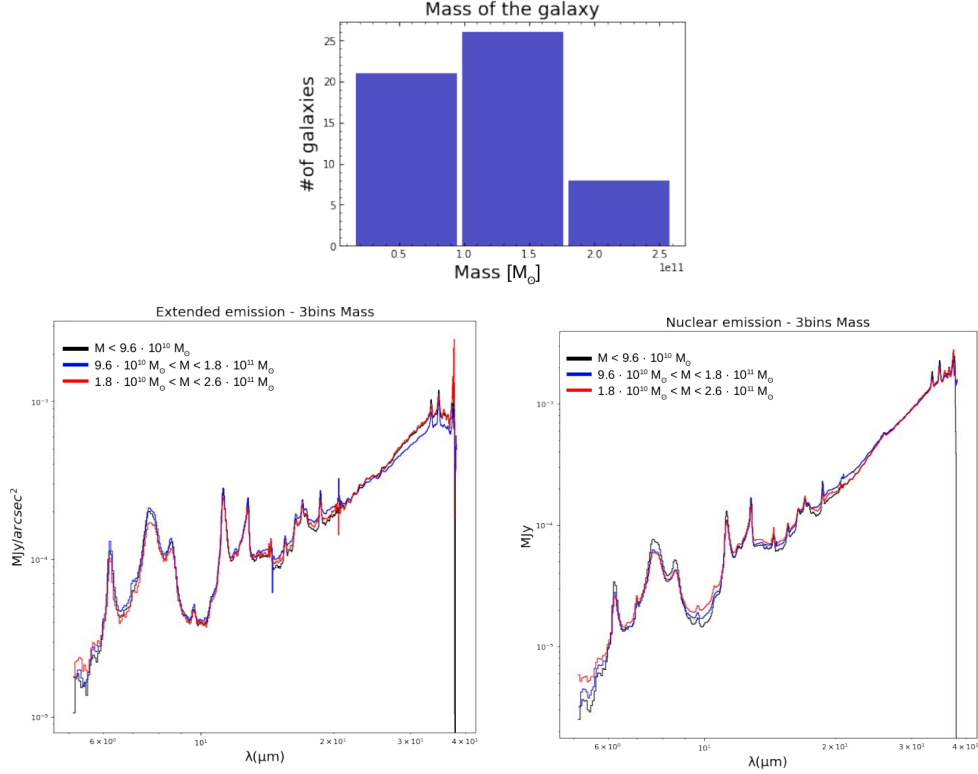


Figure 4.8: Same as in Figure 4.6 but the binning and the weighting was made according to the stellar mass

Stierwalt et al. (2013) classified the LIRGs in GOALS in five merger stages, going from 0 to 4: (0) no detected interaction, (1) early merger stage with no morphological disturbance taking place, (2) morphological disturbance gets strong, (3) the optical disks are destroyed but the 2 nuclei are still separate, (4) merged galaxies with only the structure of the disks show that there was a merger happening. We distribute the galaxies in 3 bins according to their merger stage. The first bin contains galaxies with merger stage 0, the second bin, contains galaxies with merger stage 1 and 2, and the third bin contains the galaxies with merger stage 3 and 4. In the extended emission figure, the red spectrum has slightly weaker PAH lines which could be interpreted by the PAH destruction through merger-induced shocks (Murata et al. (2017)). This is not detected on the nuclear emission. In this case, all the spectra seem very similar. Only the red spectrum shows a slightly smaller silicate absorption.

Finally, in Figure 4.10 the galaxies are classified according to their SFR. The first

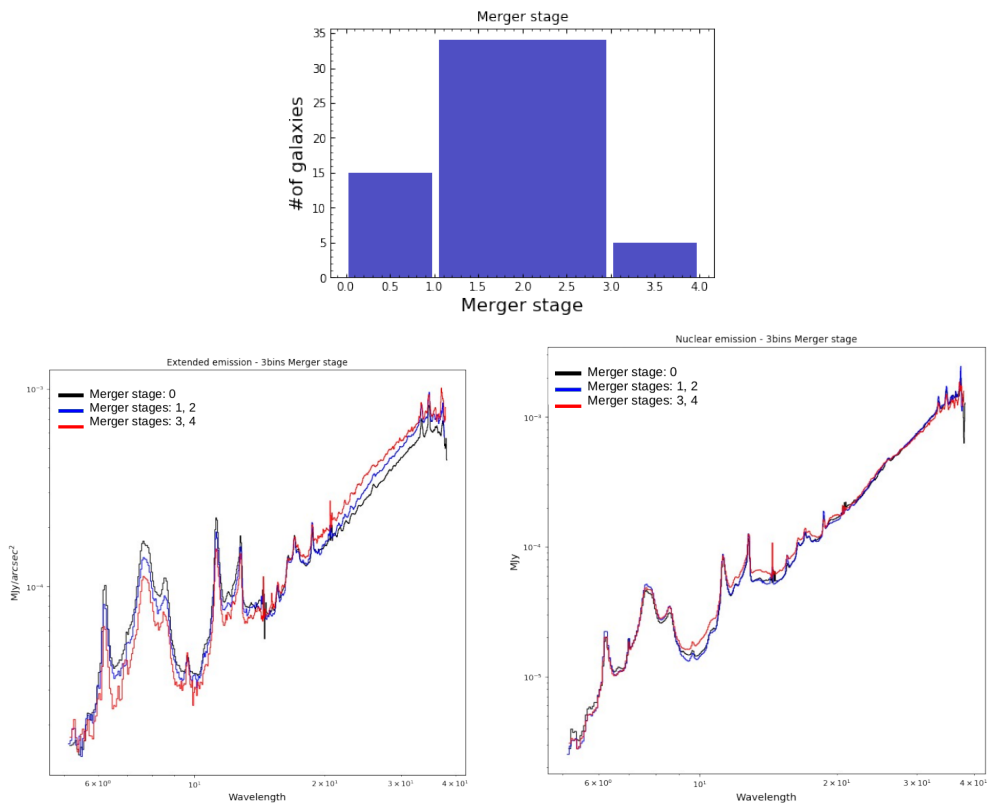


Figure 4.9: Same as in Figure 4.6 but the histogram and the weighting was made according to the merger stage of the galaxies. The galaxies of our sample are classified (Stierwalt et al. (2013)) in five merger stages, going from 0 to 4: (0) no detected interaction, (1) early merger stage with no morphological disturbance taking place, (2) morphological disturbance gets strong, (3) the optical disks are destroyed but the 2 nuclei are still separate, (4) merged galaxies with only the structure of the disks show that there was a merger happening.

bin of the histogram contains 21 galaxies with $SFR < 21.8M_{\odot}/yr$. The second bin contains 25 galaxies with $21.8M_{\odot}/yr < SFR < 43.5M_{\odot}/yr$ and the third bin contains the 4 galaxies with the highest SFR that goes up to $65.3M_{\odot}/yr$. Both for the nuclear and the extended emission spectra, we can see that the red spectrum which correspond to the galaxies with the highest SFR, has deeper silicate absorption. We could interpret this as high SFR would be more representative of a more compact starburst regions, and thus there would be more dust absorption.

4. Results

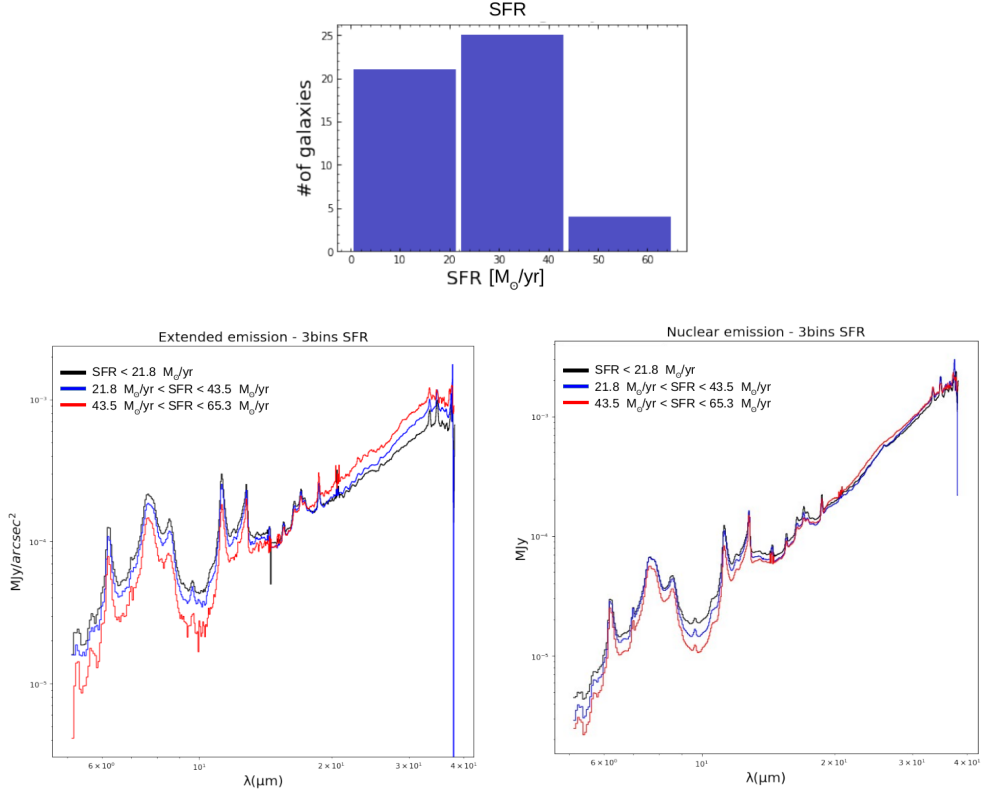


Figure 4.10: Same as in Figure 4.6 but the weighting and the binning was made according to the SFR. The red spectrum which corresponds to the galaxies with the highest SFR has the weaker silicate absorption as it is more representative of a more compact region.

4.3 PAH features, emission lines and silicate absorption

After exploring the global differences of the MIR spectra of LIRGs as a function of a number of physical properties, we now measure and quantify the PAH features, the silicate absorption features and the emission lines. We performed this analysis for our final spectra of the extended and the nuclear emission because the results could provide us information about specific properties of the ISM and inform us about what may be happening in more extended regions around the nuclei.

To measure all the features we perform a line fitting to our final spectra. The measurement of the intensity of the aromatic (PAH) features is uncertain due to the

complexity of their spectral profiles. A large fraction of their energy is distributed on the wings of these lines, which are not close to the central wavelength of the feature. Therefore, a proper extraction of the feature requires the actual band profile, which is unknown (e.g., Peters (2002); van Diedenhoven et al. (2004)). The profile that we are going to use to fit the PAH bands is the Lorentzian profile (proposed by Boulanger et al. (1998)). The considered features are centered at $\lambda = 5.7, 6.2, 7.7, 8.6, 11.3$ and $12\mu m$. The Lorentzian function is given by:

$$\mathcal{L}(x) = A \cdot \frac{\Gamma^2}{(x - x_0)^2 + \Gamma^2} \quad (4.1)$$

where A is the amplitude of the feature, which is defined as $A = \frac{1}{\pi \cdot \Gamma}$, x_0 is the center of the feature in the x axis (λ), and 2Γ is the Full Width at Half Maximum.

For the emission lines we use Gaussian functions to fit them, after a local continuum background has been measured and subtracted (see below).

$$f(x) = e^{-\frac{(x-x_0)^2}{2 \cdot \sigma^2}} \quad (4.2)$$

where x_0 is the center of the Gaussian, σ is the standard deviation and the FWHM is defined as $FWHM = 2\sqrt{2 \cdot \ln 2} \sigma$.

The considered lines are: $[Ar II]_{7\mu m}$, $[Ar III]_{9\mu m}$, $H_2S(3)_{9.65\mu m}$, $H_2S(2)_{12.28\mu m}$, $[Ne II]_{12.81\mu m}$, $[Ne III]_{15.5\mu m}$ and $[O IV]_{25.6\mu m}$. The fitting procedure is the following. First, we set a x_0 for the feature we are interested in. Then we perform a continuum subtraction using two wavelength elements before and after the feature. That is, we make a linear fit between them and we subtract this continuum from the original spectrum. We use this method for the emission lines and the PAHs. After this, their baselines are at zero. This continuum subtraction is displayed in figure 4.11. Then we continue to do the fitting of either the Lorentzian or the Gaussian functions. We show the fits to the most prominent PAHs and emission lines in Figures 4.12 and 4.13. For some galaxies not all the features could be measured due to the low signal-to-noise ratio (SNR) of the spectra. Finally, for every feature that is fitted we measure its flux, which is the integrated emission underneath the line fitting. The equivalent width of the PAH at $6.2\mu m$ was also measured.

4. Results

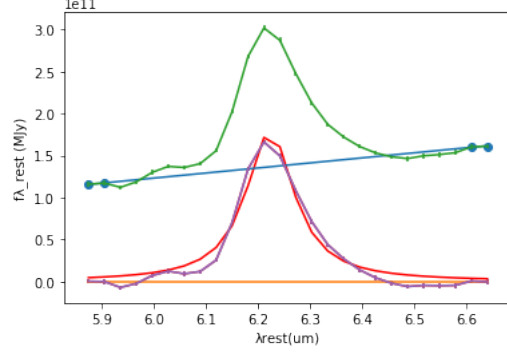


Figure 4.11: Background subtraction for the PAH line at $x_0 = 6.2\mu m$. The green spectrum shows the original spectrum before the continuum subtraction. The circles show the 4 points that were used to fit a linear continuum (blue line). After the continuum subtraction, the final spectrum is the deep purple line in which the Lorentzian is fitted (red line).

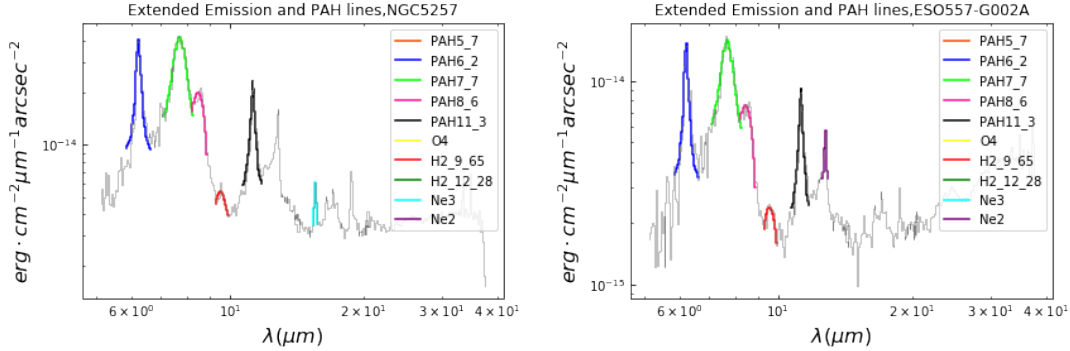


Figure 4.12: Examples of the line fitting. These are extended emission spectra of two galaxies (left NGC5257, right ESO557-G002A). The gray spectrum shows the original spectrum of these galaxies and the colored lines are the fitted functions. The strongest features of these spectra are the PAH lines at $\lambda = 6.2, 7.7, 8.6$ and $11.3\mu m$. In the second case, there is also the emission line $H_2S(3)_{9.65\mu m}$.

We also measure the strength of the silicate absorption at $9.7\mu m$, which is defined as:

$$S = \ln \frac{f_{obs}(9.7\mu m)}{f_c(9.7\mu m)} \quad (4.3)$$

where $f_{obs}(9.7\mu m)$ is the observed flux density at the peak of the $9.7\mu m$ feature and $f_c(9.7\mu m)$ is the unobscured continuum flux at the peak wavelength.

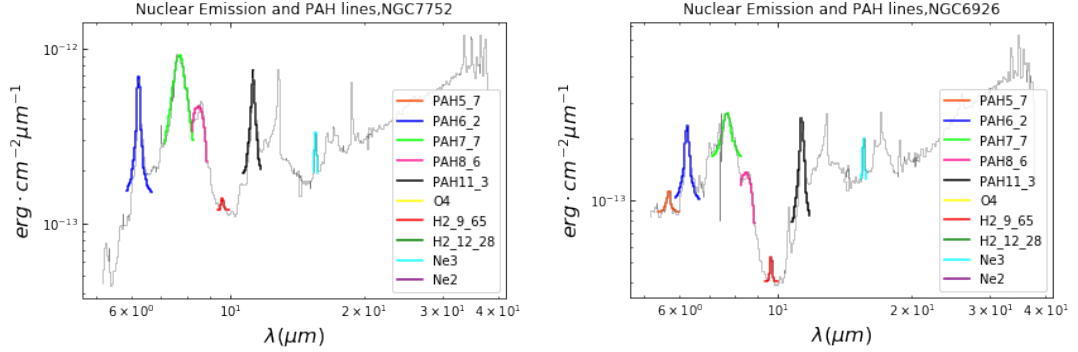


Figure 4.13: Same as in Figure 4.12 but for the galaxies: left NGC7752, right NGC6926. In these galaxies, we can also see the $[Ne\ III]_{15.5\mu m}$ line and the PAH at $5.7\mu m$.

To measure the continuum, we use three wavelength elements at $5.8\mu m$ and another three wavelength elements at $13.6\mu m$ and fit them with a power law. The representation is shown in Figure 4.14. The results of the spectral decomposition for the the galaxies in our sample as obtained by our fits are presented in Tables 6.1, 6.2 (PAH strengths, silicate strength).

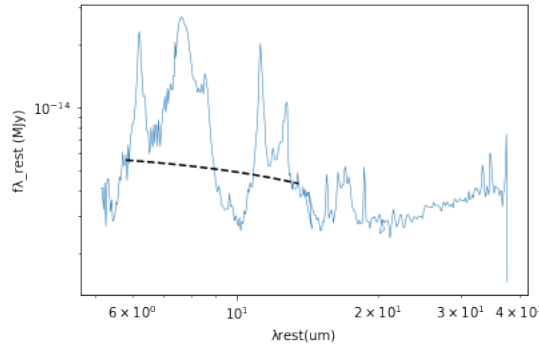


Figure 4.14: Example of the power law fitting for the silicate absorption calculation. The blue spectrum shows the original nuclear spectra of a galaxy NGC2342A. The black dashed line is the power law fit for the continuum.

After all these features are measured we can plot them in diagnostic diagrams to study the properties of the ISM. In Figure 4.14, we compare our results with the results of Stierwalt et al. (2014), who also measured PAH fluxes for the nuclear emission of 244 LIRG and ULIRG from the GOALS. To extract one dimensional spectra, they used a wavelength dependent slit aperture with a size of approximately $10''.6 \times 36''.6$ in LL

4. Results

and $3''.7 \times 9''.5$ in SL. They also did aperture corrections to their data.

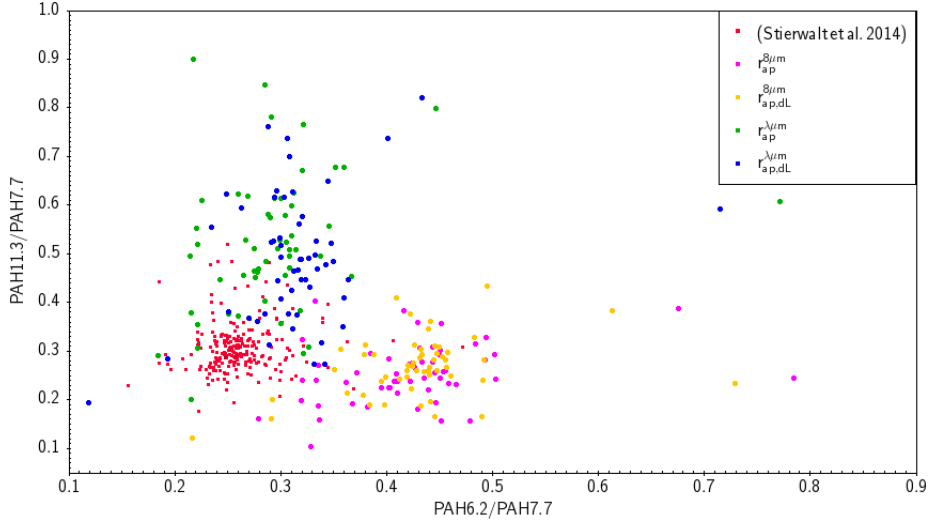


Figure 4.15: PAH diagnostics for the nuclear emission: $L(11.3\mu m)/L(7.7\mu m)$ vs. $L(6.2\mu m)/L(7.7\mu m)$. The red points correspond to the results of the Stierwalt et al. (2014) paper. The rest of the points are the results of our analysis, and their colors correspond to a different way of spectrum extraction. The blue and green data points correspond to the wavelength dependent aperture with and without distance dependency. The yellow and the pink data points correspond to a fixed aperture with and without distance dependency respectively. There is a divergence between themselves and between the data points of Stierwalt et al. (2014). This can be attributed to the different apertures that we used for the spectrum extraction.

In Figure 4.15 we show the $11.3\mu m/7.7\mu m$ PAH ratio as a function of the $6.2\mu m/7.7\mu m$ PAH ratio for the nuclear spectra, where the different colors of the data points stand for a different spectral extraction. The red data points are the results of Stierwalt et al. (2014). The blue and green data points correspond to the wavelength dependent aperture (aperture grows as the wavelength increases), with or without distance dependence, respectively. The yellow and the pink data points show the results of spectral extractions with a fixed aperture, with or without distance dependence, respectively. There seems to be a divergence between all the different data sets. Firstly, we investigate our data sets (blue, green, yellow and pink colors), where we see that the data sets that come from a fixed aperture (yellow and pink) have lower $L(11.3\mu m)/L(7.7\mu m)$ and larger $L(6.2\mu m)/L(7.7\mu m)$ than data sets where the spectra have been extracted using a wavelength dependency. This is expected because using a fixed aperture will

make some flux of the source to be lost at longer wavelengths. That is, because of the PSF increases a fixed aperture may not cover the whole flux at longer wavelengths if the source is point like. That means that when we measure the flux of the PAH bands we have a systematic flux loss in the fixed aperture extraction as we move to longer wavelengths. This will cause:

$$\frac{PAH6.2}{PAH7.7 \text{ fixed}} > \frac{PAH6.2}{PAH7.7 \text{ changing}}$$

and this is why the fixed aperture points are on the right. Similarly:

$$\frac{PAH11.3}{PAH7.7 \text{ fixed}} < \frac{PAH11.3}{PAH7.7 \text{ changing}}$$

as the PAH line at $11.3\mu m$ is at longer wavelength than the $7.7\mu m$, and the flux loss will be significant. This explains why the data points coming from a point like source and using the fixed aperture are lower and on the right on the y- and x-axes, respectively. In the case of an extended source, the effect will be the same but in this case because the wavelength dependent aperture will cover a larger physical area of the galaxy at longer wavelengths.

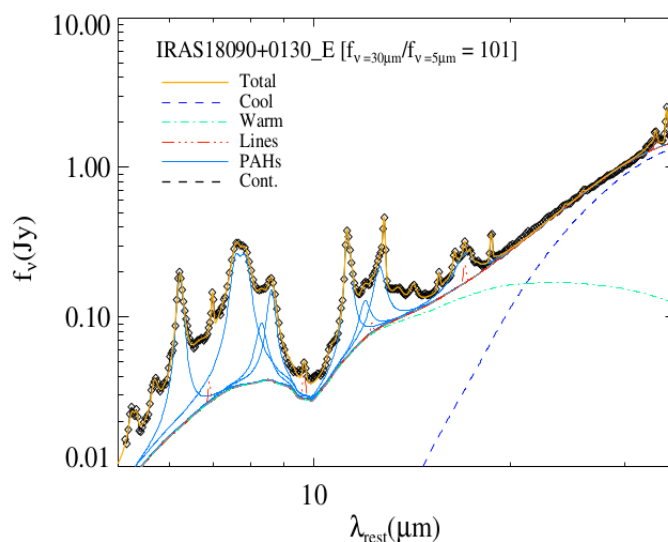


Figure 4.16: Low Resolution IRS Spectra with CAFE spectral decomposition results for the source $IRAS18090 + 0130_E$. This Figure is taken from Stierwalt et al. (2014).

4. Results

Comparing now Stierwalt et al. (2014) data points with our results, it appears that there is an offset between all our measurements and their PAH ratios. This is because in their analysis the fitting method used to estimate the continuum emission was more complex. They used the Continuum And Feature Extraction (CAFE) spectral decomposition method developed by Marshall et al. (2007) which decompose the final spectra into emission from old stellar populations, PAH features, atomic and molecular lines, and thermally heated graphite and silicate grains. Therefore, their continuum fitting is more representative of the real underlying emission than ours, which is approximated by a local linear fit. In particular, their method predicts less continuum emission and therefore their PAH fluxes are significantly larger than what we measure. This effect is particularly significant in the $7.7\mu m$ PAH feature because of the shape of the continuum. For an example, we shown in Figure 4.16 an example of the CAFE fits in Stierwalt et al. (2014). For the other PAHs our linear fit is more representative of the real underlying continuum. Another difference that is affecting the final results is that they applied an aperture correction to their spectra, which we have not implemented.

In Figure 4.17 we show a comparison between the results of our extended emission and the results of the nuclear emission by Stierwalt et al. (2014). The blue and the black triangles show the extended emission (angular and physical sizes, respectively). The red data points are the results of Stierwalt et al. (2014). We can see that the extended emission data points are located to the right of those representing the nuclear spectra, and have larger $6.2/7.7\mu m$ PAH ratios. This is an indication that the dust particles in the extended regions of the galaxy may have smaller size than in the nucleus. Also, the extended emission data points have larger $11.3/7.7\mu m$ PAH ratio which can be interpreted as a less ionized medium in the extended regions of the galaxy. The latter result is expected since the nuclear regions are expected to be associated with the nuclear starburst and maybe suffering the effects of the AGN radiation.

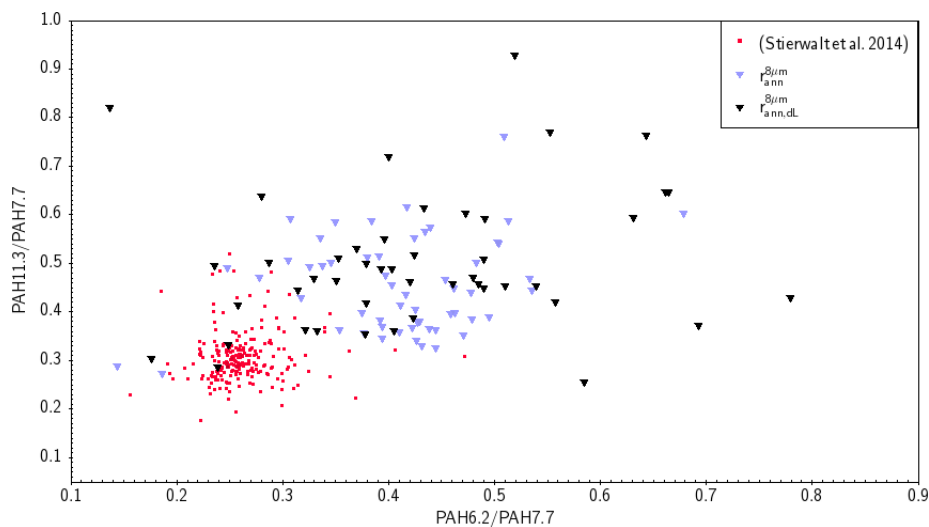


Figure 4.17: PAH diagnostics: $L(6.2\mu\text{m})/L(7.7\mu\text{m})$ vs $L(11.3\mu\text{m})/L(7.7\mu\text{m})$. This figure presents the comparison between the results of the extended emission with and without distance dependency (blue and black triangles respectively) and the results of the nuclear emission from Stierwalt et al. (2014) (red data points). We can see that the triangles are all similarly distributed in the diagram, which indicates that different extraction apertures are sampling similar regions overall. Comparing with the red data points, we can see that the extended emission triangles have larger $6.2/7.7\mu\text{m}$ PAH ratio which can be interpreted as smaller dust grains in the medium, and therefore having different ISM properties. The triangles also exhibit larger $11.3/7.7\mu\text{m}$ ratios, from which we can infer that the medium in the extended regions of galaxies are less ionized than their nucleus.

From the Figure 4.17 we can also see that the extended emission data points are in a very similar region of the parameter space. We note again that in both cases the radius and width annuli do not depend on wavelength, so any potential differences that we would see would be due to the different properties of the ISM due to the radius of the annuli. For sources that are closer than the reference luminosity distance, the annulus associated to the angular aperture extraction is located closer to the nucleus of the galaxy than the annulus associated to the distance dependent extraction. That is, because most sources are more nearby than the reference distance ($d_{A,ref} = 121\text{ Mpc}$; see section 3.1), the apertures that depended on the distance are physically further away from the nucleus in comparison to the angular size (2σ) apertures. Since the data points of the two extended emission extractions in Figure 4.17 are very close, this is an indication that the properties of the ISM do not change significantly as long as we

4. Results

measure them far from the nucleus.

The Figure 4.18 shows the diagnostic plot of the equivalent width of the $6.2 \mu\text{m}$ PAH emission feature vs the $9.7 \mu\text{m}$ silicate strength. The triangles represent the extended emission data points. Blue triangles show the distance dependent extraction while the red triangles show the angular size (2σ) extraction. The rest of the grey points show the results of the nuclear emission spectra by Stierwalt et al. (2014). The data points are divided into six categories (according to the classification of Spoon et al. (2007), Figure 1.2). The black lines show the borders of each category.

From a physics point of view, this diagnostic plot by Spoon et al. (2007) shows also the evolution of the galaxies. In the class 1A, there are the very strong AGN which have expelled the dust around them through galactic winds. If we observed a source here, we would see the hot dust component surrounding the AGN. There is no cold dust layers in the line of sight to cause extra absorption, so the spectrum is nearly featureless and the silicate absorption close to zero. The spectrum is almost entirely the hot dust continuum. Moving from class 1A to 1C (horizontal branch), star formation starts to dominate. The class 1C describes starbursts regions where PAHs are particularly strong and the silicate absorption is low. Moving now to the diagonal branch of the plot, from 1C to 3A class (see figure (1.2), there is probably a merger activity taking place. As galaxies merge, the central AGN becomes severely obscured. The spectrum that we observe in class 3A has very weak PAH features (because of the strong AGN activity), but very strong silicate absorption due to the severe obscuration of the AGN. As the obscuration reach to the highest levels, feedback from the AGN expels all the dust around it, going back to the class 1A of the diagram.

As expected, we can see that the majority of the extended data points are placed in the categories 1B, 1C, 2B and 2C, where there is no significant contribution from an AGN (obscured or unobscured). The category 2B, is characterized by the presence of PAH lines on top of a hot dust continuum. The category 1C to which the majority of the data points belong is characterized by PAH dominated spectra with the hot dust continuum nearly absent. In the category 2C, the silicate absorption is increasingly stronger. In the class 2B spectrum the PAH features appear weaker than those in the class 2C spectrum while the silicate absorption stays constant.

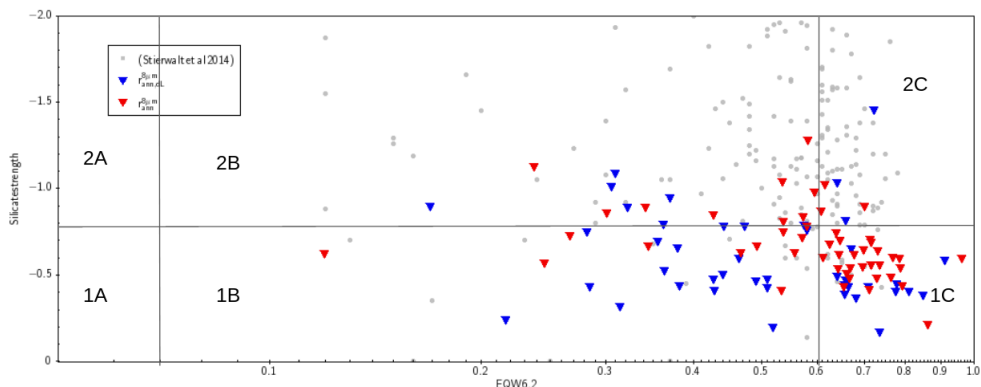


Figure 4.18: Diagnostic plot of the equivalent width of the $6.2 \mu\text{m}$ PAH emission feature vs the $9.7 \mu\text{m}$ silicate strength. The triangles represent the extended emission data points. Blue triangles show the distance dependent case while the red triangles show the 2σ case. The rest of the grey points show the results of the nuclear emission spectra by Stierwalt et al. (2014). The black continuous lines are the same lines that were used by Spoon et al. (2007) and classified the galaxies into nine categories. Our data points need only six of them: 1A, 1B, 1C, 2A, 2B, 2C.

In Figures 4.19 and 4.20 we present the wavelength dependent 2σ aperture extractions for the nuclear and extended regions of our LIRG sample. In each diagram, the faint circles around the points represent and scale with a galaxy property. In the left panel the size of the circles around the points show the merger stage of the galaxy. Smaller circles indicate little or no interaction with other galaxies. As the circles get bigger, galaxies are in more advanced stages of interaction. We can see that the circles seem to follow the diagonal branch of the Spoon et al. (2007) diagram (Figure 1.2) but the correlation is not strong enough to support that this may be the physical interpretation of the diagram. In the right panel, the size of the circles around the points show the stellar mass of the galaxy. We can see that in this case, the circles be randomly placed in the diagram, suggesting that the mass of a galaxy does not systematically affect its location in the silicate absorption - PAH $6.2\mu\text{m}$ equivalent width parameter space.

4. Results

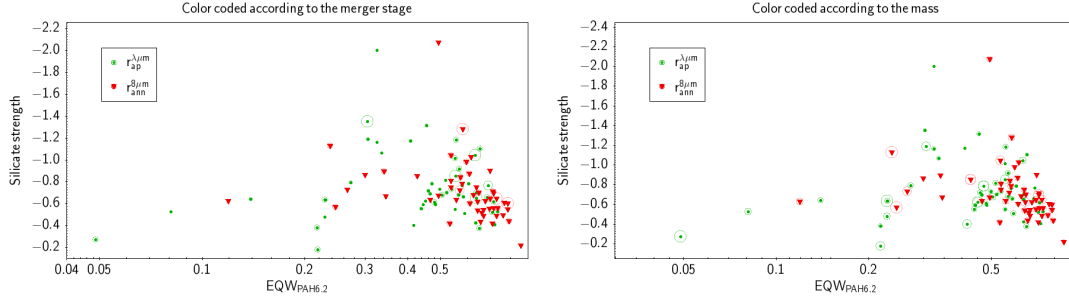


Figure 4.19: Diagnostic plot of the equivalent width of the $6.2 \mu\text{m}$ PAH emission feature vs the $9.7 \mu\text{m}$ silicate strength, showing also the dependence of a property of the galaxy. The red triangles show the 2σ extraction of the extended emission. The green data points show the nuclear emission measured by a changing aperture, not distance dependent (2σ). **Left panel:** The faint circles around the data points show the merger stage of the galaxy. No circle around a point indicate that there is no any merger happening for this galaxy. As the circles get bigger the merger is at later stages. The diagram shows no obvious relation between the merger stage and the silicate absorption or the equivalent width of the $6.2 \mu\text{m}$ PAH line. **Right panel:** Here, the circles show the mass of the galaxy. The size of the circles is proportional to the mass of the galaxy. Again, no significant relation is detected.

The Figure 4.20 shows the dependence on the AGN fraction of the galaxies, where larger circles represent larger AGN fractions. The smaller size circles are distributed over the entire parameter space, and it seems that moderate AGN fraction does not significantly affect the location of galaxies in the silicate absorption - PAH $6.2 \mu\text{m}$ equivalent width plane. On the other hand, high AGN fraction seems to affect both the extended and the nuclear data points. We can see that the largest circles have a tendency for smaller $6.2 \mu\text{m}$ PAH equivalent width. In principle, we would expect a tendency for the equivalent width of the $6.2 \mu\text{m}$ PAH line to become smaller as the AGN fraction increases, because of the presence of the hot dust continuum from the AGN in the nuclear aperture. This is also shown in the figure 4.21. However, while this is true for the nuclei of galaxies, it is interesting to note that the equivalent width of the $6.2 \mu\text{m}$ PAH feature in the extended emission also significantly depends on the AGN fraction, suggesting that the AGN is affecting the ISM properties of galaxies on large scales, over several kpc.

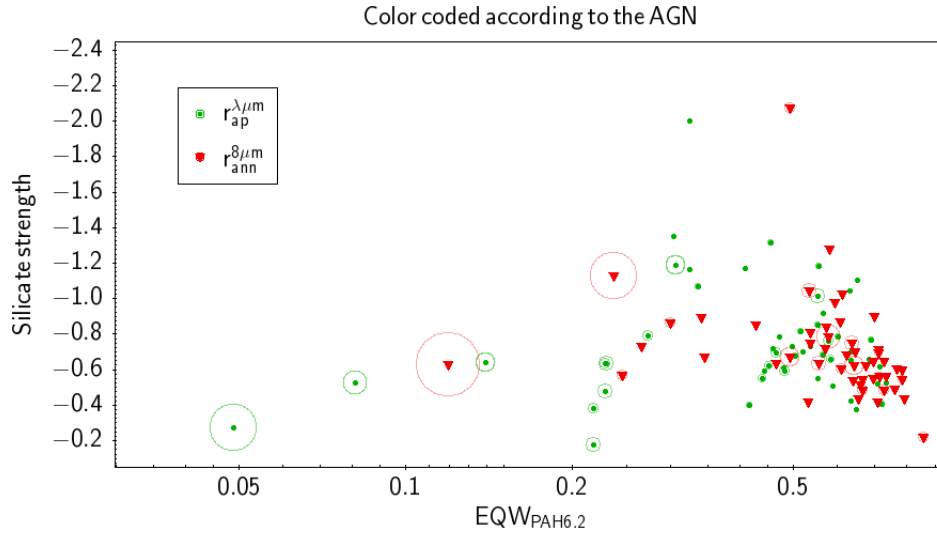


Figure 4.20: Similar as Figure 4.19, but showing the dependence on the AGN fraction. The faint circles around the data points show the AGN fraction of the galaxy. The size of the circles is proportional to the AGN fraction of the galaxy. Again, no significant relation is detected.

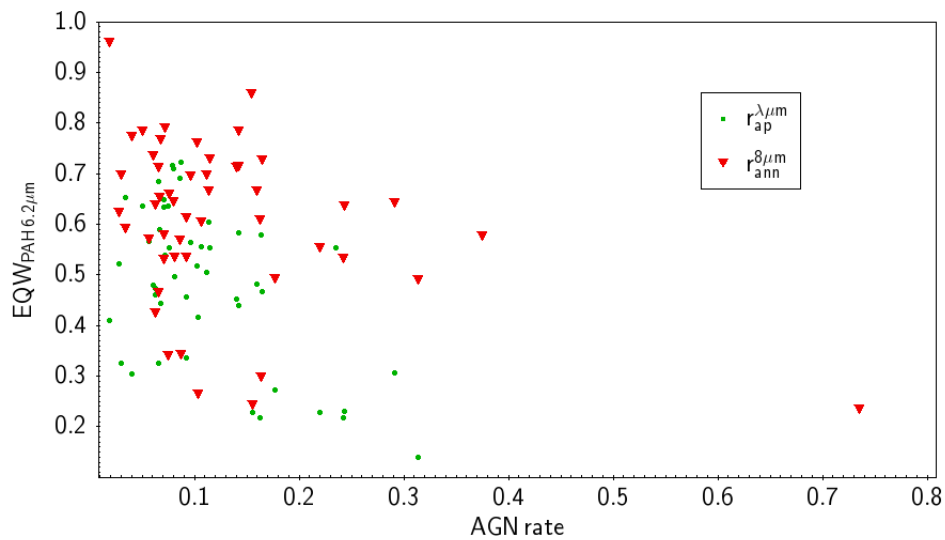


Figure 4.21: Diagnostic diagram of the equivalent width of the $6.2\mu\text{m}$ PAH line vs the AGN fraction of the galaxy. We can see a tendency for the equivalent width of the $6.2\mu\text{m}$ PAH line to become smaller as the AGN fraction increases, because of the presence of the hot dust continuum from the AGN in the nuclear aperture. This is visible both for the nuclear and the extended emission data points.

4. Results

5

Conclusions

We built the spectral cubes of 55 luminous infrared galaxies from the GOALS sample for which there are mapping observations obtained with the IRS instrument of the Spitzer Space Telescope. We extracted the spectra of the nuclear and the extended emission. The extraction was conducted following four different aperture extraction methods, which varied as a function of wavelength and also as a function of the luminosity distance of the galaxies. The GOALS galaxies cover a range of masses, silicate strengths, AGN fractions and merger stages. We have investigated the MIR properties derived from the spectral cubes and concluded the following:

- By stacking the extended emission spectra using bins, we identified that high AGN fraction could be affecting the extended emission of the galaxy. While the extended spectrum of galaxies with the highest AGN fractions exhibit the same PAH features with the spectrum coming from the lower AGN fractions, at longer wavelengths ($> 14\mu m$) the extended spectrum of the galaxies with high AGN fraction turns into a featureless continuum and it seems hotter. This suggests that the AGN could be able to heat the extended regions of the galaxy.
- The diagnostic plot of $6.2/7.7\mu m - 11.3/7.7\mu m$ PAH features shows change in the grain size and the ionization of the medium between the nuclear and the extended regions of the galaxy. We infer that the degree of ionization of the extended regions appear smaller than the ionization of the nucleus. Also, the dust grains are smaller in the extended regions of the galaxy.
- In the Spoon et al. (2007) 'fork' diagram, our extended emission data points are distributed mostly on the horizontal axis. This indicates that in the extended

5. Conclusions

regions of the galaxy there is no significant silicate absorption. Also, adding as a parameter the mass and the merger stage of the galaxies, we concluded that both, do not systematically affect the location of the data points in the silicate absorption - PAH $6.2\mu m$ equivalent width parameter space. Adding as a parameter the AGN fraction, we concluded that for the highest AGN fractions, the extended data points exhibit smaller PAH $6.2\mu m$ equivalent width which is another indication that the AGN can be indeed affecting the ISM of the extended regions of LIRGs.

- The equivalent width of the $6.2\mu m$ PAH feature of the extended emission seem to depend on the AGN fraction, again suggesting that the AGN can be indeed affecting the ISM of the extended regions of LIRGs.

6 Appendix

6. Appendix

Table 6.1: PAH features for the galaxies of our sample - angular size

Galaxy Names	RA(J2000)	DEC(J2000)	$EQW_{6.2}$	$\tau_{9.7\mu m}(\sigma)$	$6.2\mu m PAH(\sigma)$	$7.7\mu m PAH(\sigma)$	$11.3\mu m PAH(\sigma)$
NGC7752	23h46m58.62s	+29d27m32.0s	0.6467	-0.701	0.1565 (0.0011)	0.3602 (0.0043)	0.2041 (0.0005)
NGC5257	13h39m52.95s	+00d50m25.9s	0.792	-0.4373	0.7434 (0.0023)	1.6938 (0.0096)	0.6197 (0.0017)
NGC2342A	07h09m12.01s	+20d36m11.2s	0.676	-0.6216	0.4066 (0.0009)	0.9244 (0.0079)	0.5301 (0.0011)
ESO173-G015	13h27m23.79s	-57d29m21.8s	0.6994	-0.8979	1.8981 (0.0024)	4.6304 (0.037)	1.6578 (0.0067)
NGC6786A	19h11m04.37s	+73d25m32.5s	0.6106	-0.6028	0.1392 (0.0009)	0.3688 (0.0031)	0.1318 (0.0004)
IC4734	18h38m25.75s	-57d29m25.4s	0.4664	-0.6338	0.2789 (0.0021)	0.7123 (0.0072)	0.3668 (0.0011)
IC5179	22h16m09.13s	-36d50m37.2s	0.7629	-0.4912	2.1666 (0.0048)	4.876 (0.0312)	1.5936 (0.0066)
UGC03410_S	06h14m29.61s	+80d26m59.6s	0.6676	-0.5442	0.4605 (0.0015)	1.0855 (0.0066)	0.6005 (0.0014)
M+0-29-23	11h21m12.24s	-02d59m02.5s	0.4941	-2.0739	0.1455 (0.0095)	0.5877 (0.0109)	0.2885 (0.0046)
NGC5990	15h46m16.41s	+02d24m55.6s	0.4929	-0.6721	0.8652 (0.0024)	2.0353 (0.0139)	0.8226 (0.0023)
NGC5734A	14h45m11.02s	-20d54m48.6s	0.7289	-0.4855	0.6517 (0.0012)	1.3642 (0.0104)	0.5999 (0.0018)
NGC7674	23h27m56.71s	+08d46m44.3s	0.2373	-1.1285	0.2765 (0.007)	1.926 (0.0212)	0.5538 (0.0018)
NGC3256	10h27m51.30s	-43d54m14.0s	0.7859	-0.6	5.6556 (0.0095)	12.0264 (0.0913)	4.2426 (0.0182)
ESO343-IG013	21h36m10.93s	-38d32m33.0s	0.5705	-0.72	0.047 (0.0004)	0.1444 (0.0029)	0.0711 (0.0007)
NGC1365	03h33m36.40s	-36d08m25.9s	0.5791	-0.7822	8.8981 (0.0139)	20.8504 (0.1543)	7.1377 (0.0445)
NGC5734	14h45m09.04s	-20d52m13.2s	0.7863	-0.5453	1.1422 (0.0021)	2.5705 (0.0187)	0.9352 (0.0033)
NGC1068	02h42m40.72s	-00d00m47.9s	0.1195	-0.6259	4.6305 (0.0171)	15.1503 (0.0942)	7.6618 (0.0377)
NGC2342	07h09m18.07s	+20d38m10.2s	0.641	-0.539	0.3918 (0.0006)	1.0454 (0.0072)	0.4175 (0.0013)
NGC5653	14h30m10.44s	+31d12m55.8s	0.6606	-0.5124	1.3728 (0.0033)	3.1938 (0.0249)	1.2148 (0.005)
ESO557-G002A	06h31m47.20s	-17d37m16.6s	0.9618	-0.599	0.2972 (0.0012)	0.5557 (0.0065)	0.2469 (0.0006)
UGC03608	06h57m34.41s	+46d24m10.6s	0.7364	-0.5592	0.5982 (0.0013)	1.3858 (0.0079)	0.4564 (0.0013)
NGC6701	18h43m12.52s	+60d39m11.6s	0.5365	-0.8096	0.3812 (0.0012)	0.7563 (0.0081)	0.4096 (0.0016)
IRAS17138-1017	17h16m35.68s	-10d20m40.5s	0.5808	-1.2792	0.4872 (0.0029)	1.2276 (0.0066)	0.5846 (0.0037)
IC0563	09h46m21.10s	+03d04m16.3s	0.7161	-0.5609	0.2764 (0.001)	0.5981 (0.0064)	0.2692 (0.0008)
NGC1572	04h22m42.81s	-40d36m03.1s	0.2668	-0.7283	0.106 (0.0007)	0.2759 (0.0027)	0.1623 (0.0006)
NGC0828	02h10m09.53s	+39d11m24.7s	0.7299	-0.6437	1.2851 (0.0022)	3.0452 (0.025)	1.1218 (0.0042)
MRK938	00h11m06.56s	-12d06m28.2s	0.776	-6.2904	0.1729 (0.0087)	0.4142 (0.0351)	0.2555 (0.0044)
ESO244-G012	01h18m08.31s	-44d27m43.4s	0.5729	-0.8382	0.2556 (0.0008)	0.6493 (0.0041)	0.2238 (0.0009)
MCG-02-01-051	00h18m50.90s	-10d22m36.7s	0.7132	-0.7092	0.3137 (0.002)	0.734 (0.0037)	0.2787 (0.0006)
ESO264-G036	10h43m07.51s	-46d12m44.1s	0.7144	-0.693	0.3611 (0.001)	0.7099 (0.0202)	0.54 (0.0024)
ESO138-G027	17h26m43.35s	-59d55m55.2s	0.7678	-0.6059	0.542 (0.0013)	1.0957 (0.0064)	0.4282 (0.0013)
NGC6926	20h33m06.13s	-02d01m38.9s	0.6433	-0.619	0.4183 (0.0007)	0.9112 (0.0055)	0.3612 (0.0008)
NGC7591	23h18m16.25s	+06d35m09.1s	0.5363	-0.7488	0.3452 (0.0016)	0.9764 (0.0084)	0.3543 (0.0014)
NGC6786	19h10m54.01s	+73d24m36.0s	0.5326	-0.4151	0.2217 (0.001)	0.6991 (0.0042)	0.2996 (0.0008)
ESO440-IG058	12h06m51.70s	-31d56m46.4s	0.5941	-0.9798	0.1632 (0.0009)	0.4291 (0.0032)	0.2203 (0.0006)
UGC03410	06h13m57.90s	+80d28m34.7s	0.3008	-0.8608	0.042 (0.0005)	0.1367 (0.0019)	0.0809 (0.0004)
NGC7130	21h48m19.54s	-34d57m04.7s	0.5565	-0.633	0.9559 (0.0038)	2.3691 (0.0158)	1.0794 (0.0039)
NGC5135	13h25m44.02s	-29d50m00.4s	0.6381	-0.7469	0.6778 (0.0022)	1.4034 (0.0084)	0.7052 (0.0039)
NGC5257A	13h39m57.72s	+00d49m53.0s	0.6983	-0.6449	0.5238 (0.0023)	1.0948 (0.0053)	0.4227 (0.0011)
NGC6156	16h34m52.55s	-60d37m08.0s	0.8605	-0.2162	1.1073 (0.0018)	2.0761 (0.0171)	0.9732 (0.0033)
NGC2388	07h28m53.44s	+33d49m07.8s	0.625	-0.679	0.5769 (0.0014)	1.2716(0.0137)	0.5931 (0.0028)
MCG+02-20-003	07h35m41.53s	+11d36m42.1s	0.6671	-0.4862	0.1261 (0.0009)	0.3196 (0.0026)	0.1182 (0.0004)
NGC3110	10h04m02.11s	-06d28m29.5s	0.6963	-0.5514	0.7725 (0.0009)	1.97 (0.0113)	0.7559 (0.0022)
IC4687	18h13m39.80s	-57d43m30.7s	1.3157	-0.3807	0.7604 (0.0053)	1.8261 (0.011)	0.7946 (0.0018)
NGC5256 NED01	13h38m17.25s	+48d16m32.9s	0	-3.0394	0	0.3451 (0.0769)	0.1328 (0.0407)
NGC2388A	07h29m04.59s	+33d51m38.0s	0.7106	-0.4171	0.3906 (0.0006)	0.8441 (0.0059)	0.3371 (0.0008)
ESO557-G002	06h31m45.71s	-17d38m44.9s	0.3454	-0.6693	0.0498 (0.0007)	0.1791 (0.0048)	0.0845 (0.0011)
NGC7469	23h03m15.64s	+08d52m25.5s	0.5354	-1.0408	0.7429 (0.0098)	1.0949 (0.0211)	0.6597 (0.004)
UGC03351	05h45m48.03s	+58d42m03.6s	0.6141	-1.0266	0.4883 (0.003)	0.9699 (0.0091)	0.5272 (0.0013)
NGC7771	23h51m24.80s	+20d06m42.2s	0.4274	-0.8493	0.2514 (0.0014)	0.7188 (0.007)	0.4204 (0.0011)
NGC6286A	16h58m31.63s	+58d56m13.3s	0.6064	-0.8703	0.1949 (0.0019)	0.5765 (0.006)	0.2856 (0.004)
NGC7752A	23h47m04.84s	+29d29m00.5s	0.246	-0.5691	0.0554 (0.0004)	0.1605 (0.0017)	0.0804 (0.0005)
ESO221-IG010	13h50m56.92s	-49d03m18.8s	0.6548	-0.4335	0.97 (0.0029)	2.3576 (0.0182)	0.9744 (0.0025)
NGC6286	16h58m23.99s	+58d57m21.7s	0.3417	-0.8924	0.0531 (0.0012)	0.1035 (0.0016)	0.0608 (0.0005)

Table 6.2: PAH features for the galaxies of our sample - physical size

Galaxy Names	RA(J2000)	DEC(J2000)	$EQW_{6.2}$	$\tau_{9.7\mu m}(\sigma)$	$6.2\mu m PAH(\sigma)$	$7.7\mu m PAH(\sigma)$	$11.3\mu m PAH(\sigma)$
NGC7752	23h46m58.62s	+29d27m32.0s	0.2058	-1.1659	0.0591 (0.0037)	0.4269 (0.014)	0.2014 (0.0043)
NGC5257	13h39m52.95s	+00d50m25.9s	0.7381	-0.3627	0.845 (0.0013)	1.788 (0.013)	0.7915 (0.0022)
NGC2342A	07h09m12.01s	+20d36m11.2s	0.7399	-0.6244	0.364 (0.0012)	0.6747 (0.0047)	0.3615 (0.0012)
ESO173-G015	13h27m23.79s	-57d29m21.8s	-0.9840	-0.4840	1.2492 (0.6093)	0.0000	0.0000
NGC6786A	19h11m04.37s	+73d25m32.5s	0.6925	-0.3483	0.1394 (0.0017)	0.1854 (0.0037)	0.152 (0.0008)
IC4734	18h38m25.75s	-57d29m25.4s	0.4092	-0.4750	0.3046 (0.0015)	0.9423 (0.0115)	0.4788 (0.0013)
IC5179	22h16m09.13s	-36d50m37.2s	0.3428	-0.6217	3.4702 (0.0764)	11.7457 (0.1196)	3.9408 (0.0232)
UGC03410_S	06h14m29.61s	+80d26m59.6s	0.2053	-0.6447	0.1227 (0.0042)	0.5633 (0.0107)	0.2314 (0.0007)
M+0-29-23	11h21m12.24s	-02d59m02.5s	0.4542	-2.4622	0.1906 (0.0204)	1.2394 (0.0601)	0.2768 (0.0197)
NGC5990	15h46m16.41s	+02d24m55.6s	0.5420	-0.3068	0.5993 (0.0047)	1.2037 (0.0157)	0.6317 (0.0029)
NGC5734A	14h45m11.02s	-20d54m48.6s	0.8066	-0.1719	0.3003 (0.0032)	0.3507 (0.0381)	0.3025 (0.0025)
NGC7674	23h27m56.71s	+08d46m44.3s	0.4038	-0.6491	0.6038 (0.0149)	2.5061 (0.0348)	0.8676 (0.0034)
NGC3256	10h27m51.30s	-43d54m14.0s	0.2205	-0.9635	1.1707 (0.1799)	67.0000	5.7876 (0.0302)
ESO343-IG013	21h36m10.93s	-38d32m33.0s	0.3175	-0.5224	0.1128 (0.0011)	0.4183 (0.008)	0.1355 (0.0017)
NGC5734	14h45m09.04s	-20d52m13.2s	0.3697	-0.7841	0.3848 (0.0027)	0.7321 (0.0236)	0.4025 (0.0013)
NGC2342	07h09m18.07s	+20d38m10.2s	0.5848	-0.4607	1.7173 (0.004)	3.5222 (0.0265)	1.7308 (0.0028)
NGC5653	14h30m10.44s	+31d12m55.8s	0.6543	-0.3276	0.8568 (0.0008)	2.1711 (0.0121)	1.1422 (0.0029)
ESO557-G002A	06h31m47.20s	-17d37m16.6s	0.6100	-0.4084	0.231 (0.0025)	0.3285 (0.0171)	0.2385 (0.0015)
UGC03608	06h57m34.41s	+46d24m10.6s	0.3809	-0.5426	0.3374 (0.002)	0.8765 (0.0095)	0.5439 (0.0013)
NGC6701	18h43m12.52s	+60d39m11.6s	0.2317	-0.9017	0.3528 (0.0062)	1.2415 (0.0109)	0.6858 (0.0024)
IRAS17138-1017	17h16m35.68s	-10d20m40.5s	0.5808	-2.1986	0.2446 (0.0051)	0.6729 (0.0331)	0.2882 (0.0029)
IC0563	09h46m21.10s	+03d04m16.3s	1.2381	-0.7038	0.3906 (0.022)	0.0000	0.2674 (0.002)
NGC1572	04h22m42.81s	-40d36m03.1s	0.3177	-0.5567	0.1559 (0.002)	0.3633 (0.0046)	0.2063 (0.0016)
NGC0828	02h10m09.53s	+39d11m24.7s	0.2685	-0.5665	0.3101 (0.0014)	0.8873 (0.021)	0.5762 (0.003)
MRK938	00h11m06.56s	-12d06m28.2s	0.0000	-3.1232	0.0331 (0.0012)	0.4611 (0.0866)	0.7228 (0.0325)
ESO244-G012	01h18m08.31s	-44d27m43.4s	0.4335	-0.8313	0.1655 (0.0019)	0.4446 (0.0061)	0.1769 (0.0009)
MCG-02-01-051	00h18m50.90s	-10d22m36.7s	0.6169	-0.2212	0.296 (0.003)	0.6535 (0.0031)	0.3089 (0.0007)
ESO264-G036	10h43m07.51s	-46d12m44.1s	0.6589	-0.5291	0.797 (0.0022)	1.7974 (0.0125)	0.8263 (0.0049)
ESO138-G027	17h26m43.35s	-59d55m55.2s	0.6337	-0.7790	0.6791 (0.0023)	0.9197 (0.007)	0.5033 (0.0014)
NGC6926	20h33m06.13s	-02d01m38.9s	0.6270	-0.6769	0.9668 (0.0017)	2.031 (0.0102)	0.83 (0.0023)
NGC7591	23h18m16.25s	+06d35m09.1s	1.6351	-0.6728	0.5051 (0.0021)	0.7081 (0.0101)	0.374 (0.0018)
NGC6786	19h10m54.01s	+73d24m36.0s	0.4046	-0.3962	0.2283 (0.0021)	0.79 (0.0057)	0.389 (0.001)
ESO440-IG058	12h06m51.70s	-31d56m46.4s	0.5186	-0.4287	0.2046 (0.0043)	0.4839 (0.0077)	0.1763 (0.0014)
UGC03410	06h13m57.90s	+80d28m34.7s	0.9412	-1.2912	1.1616 (0.1144)	2.1255 (0.0729)	0.3319 (0.0251)
NGC7130	21h48m19.54s	-34d57m04.7s	0.3930	-0.7460	0.5716 (0.008)	0.9768 (0.023)	0.9775 (0.0022)
NGC5135	13h25m44.02s	-29d50m00.4s	0.2732	-0.6255	0.582 (0.0177)	1.1711 (0.0664)	1.1272 (0.0222)
NGC5257A	13h39m57.72s	+00d49m53.0s	0.2885	-0.4935	0.2737 (0.0027)	0.6146 (0.0136)	0.3253 (0.0077)
NGC6156	16h34m52.55s	-60d37m08.0s	0.6539	-0.1343	3.8859 (0.0084)	8.3425 (0.0742)	4.0759 (0.0106)
MCG+02-20-003	07h35m41.53s	+11d36m42.1s	0.6544	-2.5396	0.4616 (0.0062)	2.0265 (0.0331)	0.8398 (0.0026)
NGC3110	10h04m02.11s	-06d28m29.5s	0.5158	-0.3952	0.5827 (0.0053)	2.052 (0.0124)	1.0784 (0.0031)
IC4687	18h13m39.80s	-57d43m30.7s	1.8299	-0.9344	0.4868 (0.0123)	1.1909 (0.0192)	0.7611 (0.0025)
NGC5256 NED01	13h38m17.25s	+48d16m32.9s	-2.4911	-3.5851	0.0838 (0.0274)	0.0000	0.0000
NGC2388A	07h29m04.59s	+33d51m38.0s	0.7048	-0.5033	0.6325 (0.0021)	1.2471 (0.0155)	0.7426 (0.0013)
ESO557-G002	06h31m45.71s	-17d38m44.9s	0.6613	-3.9448	0.0331 (0.0012)	0.0585 (0.0313)	0.0583 (0.0037)
NGC7469	23h03m15.64s	+08d52m25.5s	0.3993	-1.4404	0.3754 (0.0514)	0.0000	0.4658 (0.0115)
UGC03351	05h45m48.03s	+58d42m03.6s	0.3463	-0.6132	0.3123 (0.0043)	0.7645 (0.008)	0.4168 (0.0009)
NGC7771	23h51m24.80s	+20d06m42.2s	1.2579	-2.0331	0.8161 (0.1056)	1.2177 (0.0326)	0.582 (0.0046)
NGC6286A	16h58m31.63s	+58d56m13.3s	0.2498	-1.0213	0.2158 (0.0021)	0.9769 (0.0142)	0.4411 (0.0033)
NGC7752A	23h47m04.84s	+29d29m00.5s	0.3387	-0.4519	0.3086 (0.0015)	0.7605 (0.0054)	0.409 (0.0014)
ESO221-IG010	13h50m56.92s	-49d03m18.8s	0.5663	-0.3978	1.3438 (0.0038)	2.9711 (0.0267)	1.5431 (0.0065)
NGC6286	16h58m23.99s	+58d57m21.7s	1.4649	-1.1598	0.6424 (0.0065)	0.5934 (0.0101)	0.2602 (0.0028)

6. Appendix

Table 6.3: Properties of the galaxies of our sample

Galaxy Names	z	d_L [Mpc]	LIR [L_\odot]	AGN fraction	SFR [M_\odot/yr]	Stellar mass [M_\odot]	Merger stage
NGC7752	0.01708	73.6	56000000000	0.08	7.7	24100000000	2
NGC5257	0.02261	108.5	267000000000	0.072	36.7	142000000000	2
NGC2342A	0.0176	78	135000000000	0	0	71000000000	1
ESO173-G015	0.00973	34	255000000000	0.03	36.7	33300000000	0
NGC6786A	0.02511	113	93400000000	0.163	11.6	114000000000	2
IC4734	0.01561	73.4	266000000000	0.066	36.9	91000000000	0
IC5179	0.01141	51.4	150000000000	0.103	20	123000000000	0
UGC03410_S	0.01308	59.7	92300000000	0.114	12.2	85500000000	1
M+0-29-23	0.0249	117	204000000000	0.177	24.9	121000000000	1
NGC5990	0.01281	64.4	163000000000	0.314	16.6	142000000000	1
NGC5734A	0.01375	67.1	67900000000	0.165	8.4	66300000000	1
NGC7674	0.02892	125	264000000000	0.735	10.4	249000000000	2
NGC3256	0.00935	38.9	437000000000	0.05	61.7	114000000000	4
ESO343-IG013	0.01906	85.8	82800000000	0.086	11.2	147000000000	3
NGC1365	0.00546	17.9	89200000000	0.375	8.3	144000000000	0
NGC5734	0.01375	67.1	108000000000	0.142	13.7	123000000000	1
NGC1068	0.00379	15.9	248000000000	1	0	144000000000	0
NGC2342	0.0176	78	188000000000	0.063	26.1	127000000000	1
NGC5653	0.01188	60.2	0	0.076	0	92800000000	0
ESO557-G002A	0.0213	93.6	163000000000	0.019	23.8	25000000000	1
UGC03608	0.02135	94.3	234000000000	0.061	32.6	96900000000	2
NGC6701	0.01323	62.4	113000000000	0.081	15.5	97700000000	0
IRAS17138-1017	0.01734	84	338000000000	0.071	46.6	153000000000	4
IC0563	0.02	92.9	68600000000	0.142	8.7	116000000000	1
NGC1572	0.02038	88.6	204000000000	0.104	27.2	201000000000	0
NGC0828	0.01793	76.3	219000000000	0.115	28.7	200000000000	4
MRK938	0.01962	84.1	319000000000	0.04	45.5	89200000000	4
ESO244-G012	0.02104	91.5	251000000000	0.057	35.1	137000000000	2
MCG-02-01-051	0.02722	117.5	470000000000	0.066	65.3	51600000000	2
ESO264-G036	0.02101	100	181000000000	0.14	23.1	245000000000	0
ESO138-G027	0.02078	98.3	276000000000	0.068	38.2	70900000000	0
NGC6926	0.01961	89.1	78300000000	0.291	8.2	195000000000	1
NGC7591	0.01653	71.4	137000000000	0.092	18.4	98100000000	0
NGC6786	0.02511	113	159000000000	0.071	21.9	130000000000	2
ESO440-IG058	0.0232	112	0	0.034	0	80300000000	2
UGC03410	0.01308	59.7	18900000000	0.164	2.4	37300000000	1
NGC7130	0.01615	72.7	254000000000	0.22	29.5	145000000000	0
NGC5135	0.01369	60.9	221000000000	0.243	24.9	127000000000	0
NGC5257A	0.02261	108.5	253000000000	0.112	33.3	159000000000	2
NGC6156	0.01088	48	112000000000	0.155	14	101000000000	0
NGC2388	0.01379	62.1	214000000000	0.028	30.9	77300000000	1
MCG+02-20-003	0.01625	72.8	0	0.16	0	24300000000	1
NGC3110	0.01686	79.5	220000000000	0.096	29.5	132000000000	1
IC4687	0.01735	81.9	228000000000	0.079	31.2	86900000000	2
NGC5256 NED01	0.02782	129	318000000000	0.235	36.2	63300000000	2
NGC2388A	0.01379	62.1	35300000000	0	0	38300000000	1
ESO557-G002	0.0213	93.6	30900000000	0.087	4.2	21700000000	1
NGC7469	0.01632	70.8	379000000000	0.242	42.7	195000000000	2
UGC03351	0.01486	65.8	223000000000	0.092	30.1	96900000000	1
NGC7771	0.01427	61.2	245000000000	0.063	34.1	237000000000	1
NGC6286A	0.01835	85.7	211000000000	0.107	28	126000000000	2
NGC7752A	0.01708	73.6	12200000000	0.156	1.5	260000000000	2
ESO221-IG010	0.01034	62.9	167000000000	0.067	23.2	130000000000	0
NGC6286	0.01835	85.7	71900000000	0.075	9.9	38400000000	2

References

- L. Armus, J. M. Mazzarella, A. S. Evans, J. A. Surace, D. B. Sanders, K. Iwasawa, D. T. Frayer, J. H. Howell, B. Chan, A. Petric, T. Vavilkin, D. C. Kim, S. Haan, H. Inami, E. J. Murphy, P. N. Appleton, J. E. Barnes, G. Bothun, C. R. Bridge, V. Charmandaris, J. B. Jensen, L. J. Kewley, S. Lord, B. F. Madore, J. A. Marshall, J. E. Melbourne, J. Rich, S. Satyapal, B. Schulz, H. W. W. Spoon, E. Sturm, V. U, S. Veilleux, and K. Xu. GOALS: The Great Observatories All-Sky LIRG Survey. *PASP*, 121(880):559, June 2009. doi: 10.1086/600092. 4
- F. Boulanger, P. Boissel, D. Cesarsky, and C. Rytter. The shape of the unidentified infra-red bands: analytical fit to ISOCAM spectra. *A&A*, 339:194–200, November 1998. 39
- K. I. Caputi, G. Lagache, Lin Yan, H. Dole, N. Bavouzet, E. Le Floch, P. I. Choi, G. Helou, and N. Reddy. The Infrared Luminosity Function of Galaxies at Redshifts $z = 1$ and $z \sim 2$ in the GOODS Fields. *ApJ*, 660(1):97–116, May 2007. doi: 10.1086/512667. 1
- T. Díaz-Santos, V. Charmandaris, L. Armus, A. O. Petric, J. H. Howell, E. J. Murphy, J. M. Mazzarella, S. Veilleux, G. Bothun, H. Inami, P. N. Appleton, A. S. Evans, S. Haan, J. A. Marshall, D. B. Sanders, S. Stierwalt, and J. A. Surace. The Spatial Extent of (U)LIRGs in the Mid-infrared. I. The Continuum Emission. *ApJ*, 723(2): 993–1005, November 2010a. doi: 10.1088/0004-637X/723/2/993. 5, 6
- Tanio Díaz-Santos, Almudena Alonso-Herrero, Luis Colina, Christopher Packham, N. A. Levenson, Miguel Pereira-Santaella, Patrick F. Roche, and Charles M. Telesco. A High Spatial Resolution Mid-Infrared Spectroscopic Study of the Nuclei and Star-Forming Regions in Luminous Infrared Galaxies. *ApJ*, 711(1):328–349, March 2010b. doi: 10.1088/0004-637X/711/1/328. 4

References

- James R. Houck, Thomas L. Roellig, Jeff Van Cleve, William J. Forrest, Terry L. Herter, Charles R. Lawrence, Keith Matthews, Harold J. Reitsema, B. T. Soifer, Dan M. Watson, Dan Weedman, Marty Huisjen, John R. Troeltzsch, Donald J. Barry, J. Bernard-Salas, Craig Blacken, Bernhard R. Brandl, Vassilis Charmandaris, Daniel Devost, George E. Gull, Peter Hall, Charles P. Henderson, S. James U. Higdon, Bruce E. Pirger, Justin Schoenwald, Greg C. Sloan, Keven I. Uchida, Philip N. Appleton, Lee Armus, Martin J. Burgdorf, Sergio B. Fajardo-Acosta, Carl J. Grillmair, Jim G. Ingalls, Patrick W. Morris, and Harry I. Teplitz. The infrared spectrograph on the Spitzer Space Telescope. In John C. Mather, editor, *Optical, Infrared, and Millimeter Space Telescopes*, volume 5487 of *Society of Photo-Optical Instrumentation Engineers (SPIE) Conference Series*, pages 62–76, October 2004. doi: 10.1117/12.550517. 4
- Chao-Ling Hung, D. B. Sanders, Caitlin M. Casey, Michael Koss, Kirsten L. Larson, Nicholas Lee, Yanxia Li, Kelly Lockhart, Hsin-Yi Shih, Joshua E. Barnes, Jeyhan S. Kartaltepe, and Howard A. Smith. A Comparison of the Morphological Properties between Local and $z \sim 1$ Infrared Luminous Galaxies: Are Local and High- z (U)LIRGs Different? *ApJ*, 791(1):63, August 2014. doi: 10.1088/0004-637X/791/1/63. 1
- F. Kemper, A. J. Markwick, and Paul M. Woods. The crystalline fraction of interstellar silicates in starburst galaxies. *MNRAS*, 413(2):1192–1199, May 2011. doi: 10.1111/j.1365-2966.2011.18204.x. 3
- Emeric Le Floch, Casey Papovich, Hervé Dole, Eric F. Bell, Guilaine Lagache, George H. Rieke, Eiichi Egami, Pablo G. Pérez-González, Almudena Alonso-Herrero, Marcia J. Rieke, Myra Blaylock, Charles W. Engelbracht, Karl D. Gordon, Dean C. Hines, Karl A. Misselt, Jane E. Morrison, and Jeremy Mould. Infrared Luminosity Functions from the Chandra Deep Field-South: The Spitzer View on the History of Dusty Star Formation at $0 < z < 1$. *ApJ*, 632(1):169–190, October 2005. doi: 10.1086/432789. 1
- Aigen Li and B. T. Draine. Infrared emission from interstellar dust. II. the diffuse interstellar medium. *The Astrophysical Journal*, 554(2):778–802, jun 2001. doi: 10.1086/323147. URL <https://doi.org/10.1086/323147>. 2

-
- B. Magnelli, D. Elbaz, R. R. Chary, M. Dickinson, D. Le Borgne, D. T. Frayer, and C. N. A. Willmer. The $0.4 < z < 1.3$ star formation history of the Universe as viewed in the far-infrared. *A&A*, 496(1):57–75, March 2009. doi: 10.1051/0004-6361:200811443. 1
- B. Magnelli, D. Elbaz, R. R. Chary, M. Dickinson, D. Le Borgne, D. T. Frayer, and C. N. A. Willmer. Evolution of the dusty infrared luminosity function from $z = 0$ to $z = 2.3$ using observations from Spitzer. *A&A*, 528:A35, April 2011. doi: 10.1051/0004-6361/200913941. 2
- J. A. Marshall, T. L. Herter, L. Armus, V. Charmandaris, H. W. W. Spoon, J. Bernard-Salas, and J. R. Houck. Decomposing Dusty Galaxies. I. Multicomponent Spectral Energy Distribution Fitting. *ApJ*, 670(1):129–155, November 2007. doi: 10.1086/521588. 44
- J. Melbourne, D. C. Koo, and E. Le Floch. Optical Morphology Evolution of Infrared Luminous Galaxies in GOODS-N. *ApJ*, 632(2):L65–L68, October 2005. doi: 10.1086/498019. 1
- Katsuhiro Murata, Rika Yamada, Shinki Oyabu, Hidehiro Kaneda, Daisuke Ishihara, Mitsuyoshi Yamagishi, Takuma Kokusho, and Tsutomu Takeuchi. A relationship of polycyclic aromatic hydrocarbon features with galaxy merger in star-forming galaxies at $z < 0.2$. *Monthly Notices of the Royal Astronomical Society*, 472, 07 2017. doi: 10.1093/MNRAS/STX1902. 36
- Miguel Pereira-Santaella, Almudena Alonso-Herrero, George H. Rieke, Luis Colina, Tanio Díaz-Santos, J. D. T. Smith, Pablo G. Pérez-González, and Charles W. Engelbracht. Local Luminous Infrared Galaxies. I. Spatially Resolved Observations with the Spitzer Infrared Spectrograph. *ApJS*, 188(2):447–472, June 2010. doi: 10.1088/0067-0049/188/2/447. 4
- Wouter Peters. *Polycyclic aromatic hydrocarbons and dust in regions of massive star formation*. PhD thesis, University of Groningen, December 2002. 39
- D. B. Sanders and I. F. Mirabel. Luminous Infrared Galaxies. *ARA&A*, 34:749, January 1996. doi: 10.1146/annurev.astro.34.1.749. 1

References

- H. W. W. Spoon, J. A. Marshall, J. R. Houck, M. Elitzur, L. Hao, L. Armus, B. R. Brandl, and V. Charmandaris. Mid-Infrared Galaxy Classification Based on Silicate Obscuration and PAH Equivalent Width. *ApJ*, 654(1):L49–L52, January 2007. doi: 10.1086/511268. 3, 4, 34, 46, 47, 51
- S. Stierwalt, L. Armus, J. A. Surace, H. Inami, A. O. Petric, T. Diaz-Santos, S. Haan, V. Charmandaris, J. Howell, D. C. Kim, J. Marshall, J. M. Mazzarella, H. W. W. Spoon, S. Veilleux, A. Evans, D. B. Sanders, P. Appleton, G. Bothun, C. R. Bridge, B. Chan, D. Frayer, K. Iwasawa, L. J. Kewley, S. Lord, B. F. Madore, J. E. Melbourne, E. J. Murphy, J. A. Rich, B. Schulz, E. Sturm, T. Vavilkin, and K. Xu. Mid-infrared Properties of Nearby Luminous Infrared Galaxies. I. Spitzer Infrared Spectrograph Spectra for the GOALS Sample. *ApJS*, 206(1):1, May 2013. doi: 10.1088/0067-0049/206/1/1. 3, 4, 32, 36, 37
- S. Stierwalt, L. Armus, V. Charmandaris, T. Diaz-Santos, J. Marshall, A. S. Evans, S. Haan, J. Howell, K. Iwasawa, D. C. Kim, E. J. Murphy, J. A. Rich, H. W. W. Spoon, H. Inami, A. O. Petric, and V. U. Mid-infrared Properties of Luminous Infrared Galaxies. II. Probing the Dust and Gas Physics of the GOALS Sample. *ApJ*, 790(2):124, August 2014. doi: 10.1088/0004-637X/790/2/124. 41, 42, 43, 44, 45, 46, 47
- B. van Dierendonck, E. Peeters, C. Van Kerckhoven, S. Hony, D. M. Hudgins, L. J. Allamandola, and A. G. G. M. Tielens. The Profiles of the 3-12 Micron Polycyclic Aromatic Hydrocarbon Features. *ApJ*, 611(2):928–939, August 2004. doi: 10.1086/422404. 39